# High Performance Curtain Wall Mullion Section Design with Various Densities of Gyroid

by

Min Jeong Kang

Bachelor of Engineering in Civil Engineering
The Cooper Union for the Advancement of Science and Art, 2015

Submitted to the Department of Civil and Environmental Engineering in Partial Fulfillment of the Requirement for the Degree of

Master of Engineering in Civil and Environmental Engineering
at the
Massachusetts Institute of Technology

September 2016



Signature of Author: Signature redacted
Department of Civil and Environmental Engineering
August 12, 2016

Certified By: Signature redacted
Caitlin T. Mueller
Assistant Professor of Architecture, Civil and Environmental Engineering
Thesis Advisor

Certified By: Signature redacted
Zhao Qin
Research Scientist, Civil and Environmental Engineering
Thesis Co-Advisor

Accepted By: Signature redacted
Jesse Kroll
Professor of Civil and Environmental Engineering
Chair, Graduate Program Committee

# High Performance Curtain Wall Mullion Section Design with Various Densities of Gyroid

by

Min Jeong Kang

Submitted to the Department of Civil and Environmental Engineering on August 12, 2016 in Partial Fulfillment of the Requirements for the Degree of Master of Engineering

## Abstract

The thermal bridge problem in building façades has become a topic of interest as the energy performance of building enclosure design required improvements with a global lead in sustainable building design. Curtain wall façade systems are widely used for recent high-rise buildings, and the thermal bridge issue occurs mainly within the aluminum frame of the curtain wall system. In addition to the thermal bridging effects, the conventional curtain wall façade designs have limitations in increasing the stiffness of the mullion. As to address the lack of an innovative solution to solve both issues, this thesis proposes utilizing a cellular structure in mullion design. In particular, this thesis has selected a single-gyroid structure, which is an open cell foam structure that has the minimum surface area necessary to span a region of space.

The thesis explores various aspects of the application that extend from a rapid modeling method of gyroid structure, experiments, and simulations along with theoretical values for mechanical and thermal properties of gyroid, to topology optimization of the various densities of gyroid in the composite structure. The results are expected to improve the curtain wall designs with future experimental verifications.

Thesis Supervisor: Caitlin T. Mueller
Title: Assistant Professor of Architecture and Civil and Environmental Engineering

## Acknowledgements

First, I would like to express my gratitude to Professor Caitlin Mueller for her guidance with this thesis and invaluable support. She helped me to be exposed to various fields, and directed me in the right direction when needed for this thesis to be completed.

I would also like to thank Zhao Qin, a research scientist in LAMM Group with Professor Markus J. Buehler. His knowledge in gyroid and guidance in research helped me in modeling complex geometries and conducting various experiments.

I would like to thank members in Building Technology Group and LAMM Group at MIT for their helpful guidance and assistance with their expertise in the various topics. Their insightful comments and encouragement truly helped me to continue the research.

Also, I would like to thank Dr. Xiaolu Hsi and Dr. John H. Lloyd for their support and encouragement. Their passionate advice and help motivated me to continue to strive during this difficult year.

Last but not the least, I would like to thank my family for their constant support in my education and my life in general.

# Table of Contents

# List of Figures

# List of Tables

# Nomenclature

| Symbol | Meaning |
|---|---|
| $A$ | Area |
| $A_{t,i}$ | Transformed area of a slice |
| $C_1$ | The coefficient of the scaling relation in Eq. 4.1 |
| $E_s$ | Young's modulus of the bulk material used for gyroid cell |
| $I_{global}$ | Area moment of inertia of the entire composite structure |
| $I_{t,n.a.,i}$ | Area moment of inertia of a transformed slice relative to its neutral axis |
| $J_1$ | Structural performance measure or objective 1 |
| $J_2$ | Thermal performance measure or objective 2 |
| $P^*$ | Property of gyroid |
| $P_s$ | Property of the bulk material used for solid gyroid cell |
| $V_{gyroid}$ | Volume of gyroid |
| $V_{total}$ | Total volume |
| $V_{void}$ | Volume of void |
| $d_i$ | Distance between the centroid of a slice and the centroid of the composite structure |
| $k_{cf}$ | Thermal conductivity of fluid in gyroid |
| $k_{cs}$ | Thermal conductivity of the bulk material used for solid gyroid cell |
| $k_{eff,c}$ | Thermal conductivity of composite gyroid, or effective thermal conductivity |
| $k_{eff}$ | Effective thermal conductivity, or thermal conductivity of a composite gyroid |
| $k_f$ | Thermal conductivity of fluid, (or air in this thesis) |
| $k_s$ | Thermal conductivity of solid in gyroid |
| $l_1$ | Length of resistor in the direction of the heat flow |
| $l_2$ | Length of resistor, perpendicular to the direction of the heat flow |
| $w_1$ | Weight for the objective 1 |
| $w_2$ | Weight for the objective 2 |
| $w_{air}$ | Weight of air |
| $w_{gyorid}$ | Weight of gyroid |
| $y_c$ | y-coordinate of a centroid of the composite structure |
| $y_i$ | y-coordinate of a centroid of a slice |
| $\lambda^*$ | Thermal conductivity of gyroid, used in Eq. 2.6 |
| $\lambda_s$ | Thermal conductivity of the bulk material used for solid gyroid cell, used in Eq. 2.6 |
| $\rho^*$ | Density of gyroid |
| $\rho_s$ | Density of the bulk material used for gyroid cell |
| $\sigma_C$ | Compressive strength of gyroid |
| $\sigma_T$ | Tensile strength of gyroid |

| | |
|---|---|
| $\sigma_{Ts}$ | Tensile strength of the bulk material used for gyroid cell |
| $A$ | Area perpendicular to the direction of the heat flow |
| $F$ | Composite function used for optimization or the performance measure |
| $n$ | In Eq. 4.2, an exponential value of a relative density in the scaling relation; In Chapter 5, the ratio of the Young's moduli of the different gyroid slices. |
| $E$ | Young's modulus |
| $Q$ | Heat flux |
| $R$ | Thermal resistance |
| $T$ | Temperature |
| $w$ | Width of resistor, perpendicular to the direction of the heat flow |
| $\varepsilon$ | Relative density |
| $\phi$ | Porosity |

# Chapter 1. Introduction

This chapter introduces curtain wall design and several commonly used performance measures. This thesis recognizes the design limitations of the conventional curtain wall designs currently available in the market in the perspective of high performance both structurally and thermally.

## 1.1. Curtain Wall Design and Performance Measures

In the recent decades, as the transparency in the building facade became preferable among architects and building designers, the curtain wall system has been widely used and became one of the most modern facades used since its first application in 1918, for the Hallidie Building, designed by James Polk. Even though the curtain wall is often thought to be only metal frames supporting glass panels, it means any non-gravity-load-bearing wall (Brock 2005). A curtain wall can use wood composite frames, fiberglass frames, vinyl frames, metal frames and others. Some of the types of curtain wall systems are the stick system, the ladder system, the unitized system (modular system), the I-beam wall, and the pressure wall. Figure 1.1 shows the exterior of the Hallidie Building and an example of the contemporary curtain wall façade building, L.A. Live Tower and Residences in Los Angeles.

This thesis is concerned with the frame that supports the curtain wall glazing, often called the mullions (which can be vertical or horizontal). These are of interest because they play both a structural and thermal role: they transmit wind loads from the glazing panels to the main building structure, and they form part of the building's insulating envelope. Due to their structural requirements, mullions are the thermal weak point in contemporary curtain wall design, and often constitute what is known as a thermal bridge between the interior and exterior of the building. This chapter will discuss this issue with the quantitative metrics described in the next page.

A

B

***Figure 1.1**: An example of the early curtain wall design in 1918 and an example of the contemporary curtain wall design: the Hallidie Building in San Francisco, CA (A) (Courtesy of American Institute of Architects, San Francisco Chapter; Image retrieved from http://aiasf.org/about/history/); L.A. Live Tower and Residences in Los Angeles, CA (B) (Courtesy of Devlin, Katy; Image retrieved from http://glassmagazine.com/article/commercial/greatglazing-la-live-tower-and-residences-118919).*

In the building envelope design, three basic thermal performance parameters are often used to measure energy efficiency: thermal transmittance, solar heat gain coefficient (SHGC), and condensation resistance factor (CRF). Thermal transmittance is a measure of heat flow per unit time, area and temperature difference. More often, to represent the thermal transmittance, U-factor (U-value) is expressed in BTU/hr. sqft. °F, or the reciprocal of the U-value, R-value is commonly used as a whole number with a unit of hr. sqft. °F/BTU. In practice, U-factor is utilized by the building engineer for code compliance, equipment sizing and energy performance modeling. Model Energy Codes such as ASHRAE 90/1 and IECC provide prescriptive maximums. SHGC is a dimensionless ratio of the total visible infrared and ultraviolet energy flowing through glazing, divided by incident energy. CRF is a dimensionless ratio of surface temperature to an ambient temperature difference. In addition to the three thermal performance parameters mentioned above, often the visible transmittance (VT), the percentage of visible light transmitted through the glazing, is often used in the field as a critical measure of performance. This thesis uses only the R-value to evaluate the thermal performance of each frame model, since

the other three performance measurements (SHGC, CRF, and VT) rely heavily on the glazing or glass type, less on the framing.

## 1.2. Conventional Curtain Wall Designs and Their Limitations

One of the most prevalent curtain wall facade systems is the unitized aluminum frame for its strength, lightweight, fast construction and easy maintenance. However, the aluminum frame is highly conductive so that it can transfer a significant amount of heat between the interior and the exterior side of a structure. Typical R-values for thermally-broken commercial aluminum windows and curtain walls are about 2 or 3; even the triple-glazed, thermally broken, Low-E coated systems available in the United States' market are around 5 or 6 (Straube 2008). Most of the commercially available, so-called "high-performance" curtain walls typically stay around that number, with the best of R-9. With the need for more energy-efficient building enclosure design, curtain wall systems with higher R-values are either recently developed or currently under research. Fig. 1.2 illustrates the ranges of effective overall wall R-values for different designs.

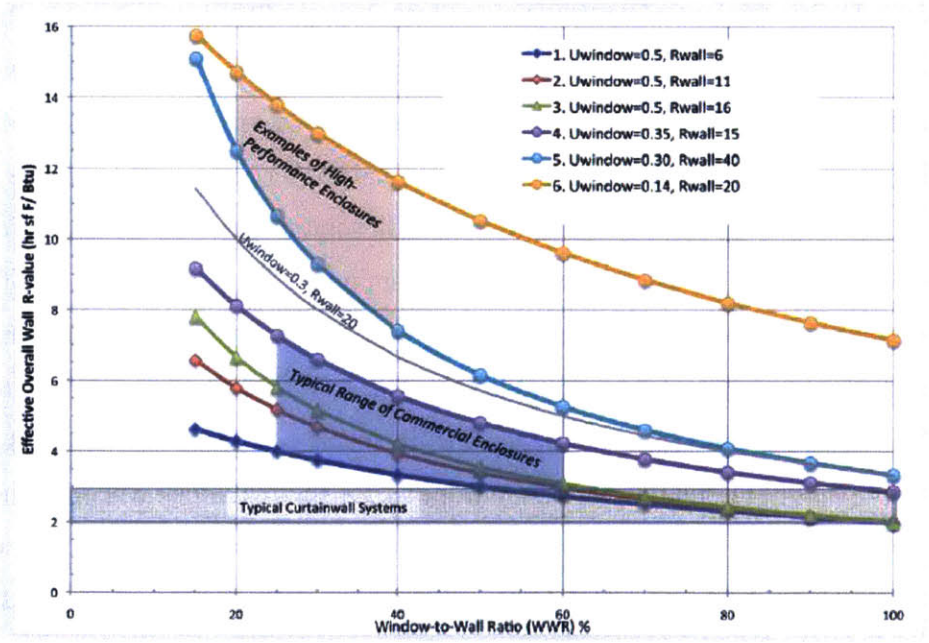


***Figure 1.2:*** *Graph Depicting Different Scenarios of Curtain Wall Facade (Courtesy of Straube 2008)*

In a curtain wall design, a wind load on the glass panels, which is then transferred to the vertical mullion, is the major structural design load. The vertical mullion is designed to have at least a

certain stiffness to resist the load; in practice, the curtain wall facade designers use the deflection limit of L/175 for a typical 12' floor-to-floor height vertical mullion design as an industry standard (Brenden 2006). Moreover, the majority of design guidelines for the curtain wall facade are based mostly on experience and basic engineering logics, thus emphasizing extra structural tests and thorough performance analysis required when the design is "out of the norm." A conventional way to increase the stiffness of the vertical mullion is to increase the depth of the mullion: most of the large-scale glass-aluminum curtain wall manufacturing companies show various sizes of vertical mullion profiles in their sales pamphlets. Increasing the depth of the vertical mullion can be undesirable for architects and owners since enlarging the mullion depth can reduce the usable/rentable space, and therefore, the profit of the building. In the case of a blast design, where the structural loads on the façade and the mullions are of a larger magnitude, the degrees of freedom in floor plan design can decrease the profit.

An example of a typical vertical mullion profile can be found in Fig. 1.3. The basic outline of the vertical mullion of 2500 UT Unitwall System® by Kawneer is prevalent among the currently available designs for its efficiency in production and its clean profile; the products in the market vary in the details of the section, such as the dimensions of the mullion, the connections, and the inside details of the aluminum extrusion. Contemporary mullions employ what is called a thermal break, which insulates across the envelope thermal barrier between the outside and inside of the mullion. Most of the available thermal break solutions exhibit the similar outline of the vertical mullion but with the details inside of the aluminum extrusion changed. As for some examples of currently available thermal break solutions in the US' market, the followings are: TU24650 Series storefront system® by Tubelite Inc. (Fig. 1.4A), standard foam insulated mullions by Starmark Windows (Fig. 1.4B), and a triply insulated window by Glo Windows (Fig. 1.4C). More popular thermal break solutions utilize the thermal break where the heat flow is expected to occur, typically nearby where the glass panels are connected or within the aluminum extrusion (Fig. 1.4A and 1.4C). Others attempt to use foam materials such as polyurethane foam within the mullions (Fig. 1.4B). These solutions may thermally perform better than the conventional designs, and yet, the majority of these thermally improved curtain wall designs remain to have the typical overall curtain wall mullion profiles that are similar to each other. Moreover, the thermal break solutions do not necessarily consider improvement in the structural performance.

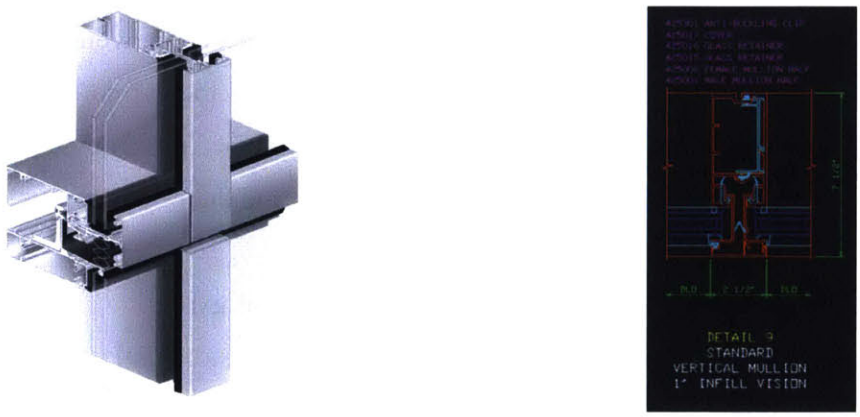


***Figure 1.3:*** *2500 UT Unitwall System® by Kawneer (Drawing Courtesy of Kawneer)*

A. B. C.

***Figure 1.4.*** *Examples of Thermal Break Solutions: TU24650 Series storefront system® by Tubelite Inc. (A) (Courtesy of Tubelite 2016); a standard foam insulated mullions by Starmark Windows (B) (Courtesy of Starmark Windows 2016); and a triply insulated window by Glo Windows (C) (Courtesy of Glo Windows 2016).*

## 1.3. Problem Statement

The conventional curtain wall design has two major issues: thermal bridging effect in aluminum framing and design limitation due to structural performance of the aluminum extrusion. Currently available thermal break solutions do not necessarily consider improving the structural performance of the mullion.

## 1.4. Research Goals

This thesis seeks to increase both structural and thermal performance of a conventional curtain wall mullion design by utilizing a specific cellular structure known as the gyroid. The study covers various aspects of the gyroid in the design application, expressed as follows:

(i) Define the scaling relations for both structural properties and thermal properties of gyroid.

(ii) Construct a rapid, parameterized digital modeling method for gyroid.

(iii) Optimize the topology of various densities of gyroid for both structural performance and thermal performance.

## 1.5. Thesis Organization

This thesis is divided into six chapters: 1) Introduction, 2) Literature Review, 3) Modeling and Materialization, 4) Assessment via Physical Experiments and Simulation, 5) Design and Optimization of Mullion System, 6) Conclusion.

Chapter 2 introduces cellular structures, including gyroid structure, with their expected advantages of usage in façade mullion.

Chapter 3 explores several digital modeling methods and 3D printing techniques to produce physical models for gyroid.

Chapter 4 focuses on finding structural properties and thermal properties of different densities of gyroid based on theories, computational simulations, and physical experiments.

Chapter 5 evaluates different topologies of gyroid with varying densities and illustrates the bi-objective optimization process conducted in the study.

Chapter 6 summarizes the work done in the thesis and presents the potential impact of these contributions in curtain wall façade mullion design.

# Chapter 2. Literature Review

The objective of this chapter is to present existing work on curtain wall design optimization. In addition, this chapter introduces cellular structures, including gyroid, which are used in this study as a solution the design problem addressed in the previous chapter.

## 2.1. Previous Optimization Studies on Curtain Wall Design

For building facade mullion design, some architects have performed optimization studies in a more holistic design point of view. In the case of the Shanghai Tower facade design by Gensler, for example, the position of the walls and the profile of the entire building were varied and analyzed for building efficiency and energy performance as well as wind load distribution of a significant portion of the exterior facade (Zeljic 2010). However, the design optimization study in both structural performance and the thermal performance of the curtain wall facade is not pursued enough, especially for the component design. In his article about component optimization design, DeGanyar aims to minimize the material in framing to achieve a lightweight facade system has been attempted with the structural optimization method (DeGanyar 2012). With the objective to optimize for the structural performance, he further designs three different components of curtain wall facade frame: anchor, vertical mullion, and a split mullion in unitized frame (Fig. 2.1); yet, he only considers the structural performance, not the thermal performance or the thermal bridging effects in the framing. As an example for evaluating thermal performance of facade component design, Carbary and Fibys, in their article, compares thermal performances of four basic types of curtain wall glazing systems: 1) insulating glass which are mechanically fixed in gaskets, 2) 4-sided structural silicone glazed with wet weather-seals, 3) 4-sided structural silicone glazed with dry gasket weather-seal, and 4) hybrid glazing system (structurally clamped). Then, Carbary and Fibys assigned the relative rankings for the models, by averaging the ranking the overall façade U value, interior profile temperature, and the interior glass temperature. And yet again, the models are only compared for thermal performance not for both structural performance and the thermal performance.

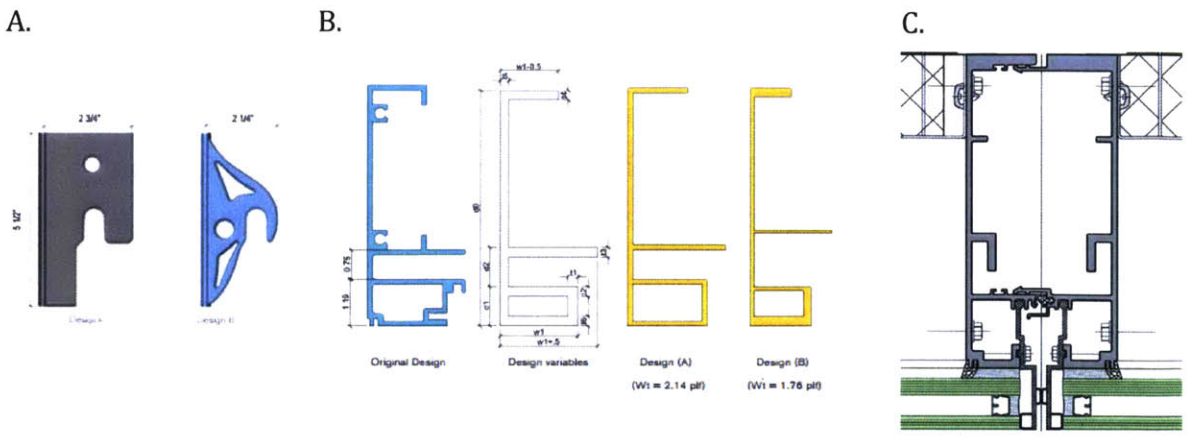


***Figure 2.1.*** *Optimized Curtain Wall Façade Components: Hook (A), Split Mullion (B), and Assembly of the Split Mullions (C) (Courtesy of DeGanyar 2012)*

## 2.2. Design Inspiration

To solve this design problem of optimizing the structural and thermal performance of façade mullion design, an innovative structural idea inspired from design in nature is tested for its feasibility and performance in this study. In nature, mammals often use fur that traps air against the skin to reduce: in other words, the air pockets created against their skin act as an insulation layer and reduce heat loss (Pawlyn 2011). This idea is not new in design in that a similar idea of using air as insulation was used for a greenhouse roof design, SolaRoof, which utilizes 750 mm-deep cavities filled with bubbles as an insulation layer. The bubbles, roughly 6 mm diameter made of a mixture of surfactants, perform as equivalent to the air pockets in furs of mammals. The SolaRoof is claimed to reduce the heat loss by ten times as compared to standard double polyethylene covered greenhouses and by 15 times to a single glass covered greenhouse (SolaRoof 2016). Likewise, this study attempts to apply the similar principle of using the air pockets as insulting layers in curtain wall façade mullion design.

## 2.3. Cellular Structures

To achieve such design that can create small air pockets, cellular structures are studied initially for their porous structure with the capacity to capture air within the structure. Cellular structures, or cellular solids, mean clusters of small compartments or "an assembly

of cells with solid edges or faces, packed together so that they fill space" (Gibson et al. 1997). Some of the common examples of cellular solids that can be found in nature are honeycomb, cancellous bone, and coral.

### 2.3.1. Types of Cellular Structures

Cellular solids are often categorized into two by whether each cell is enclosed or not: open cell and closed cell. Cellular solids by definition include both orderly structures, such as honeycomb (Fig. 2.2), and randomly filled structures, such as sponge (Fig. 2.3). In this study, more structurally ordered cellular structure is preferred not only for the ability to control the density but also for the regularity of the structure.

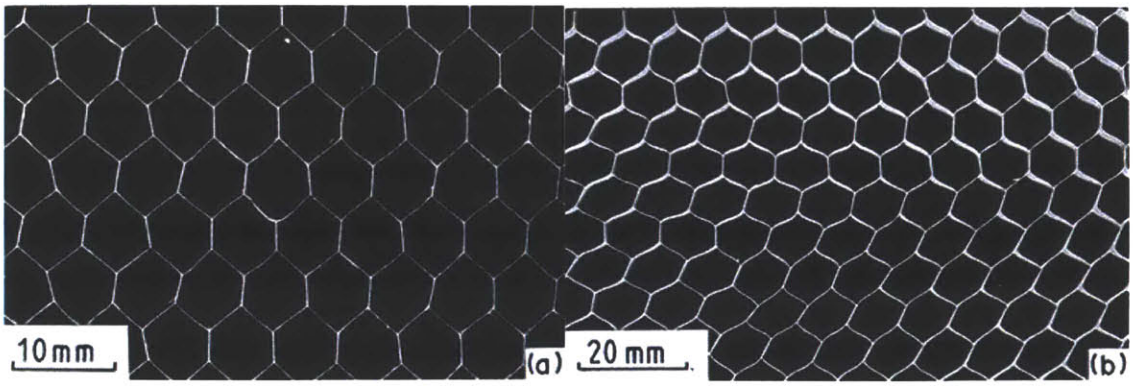


***Figure 2.2.*** *Examples of Orderly Cellular Solids: Aluminum (Left) and Paper-phenolic Honeycombs (Right) (Courtesy of Gibson et al. 1997, Image retrieved from https://lornagibson.org/research).*

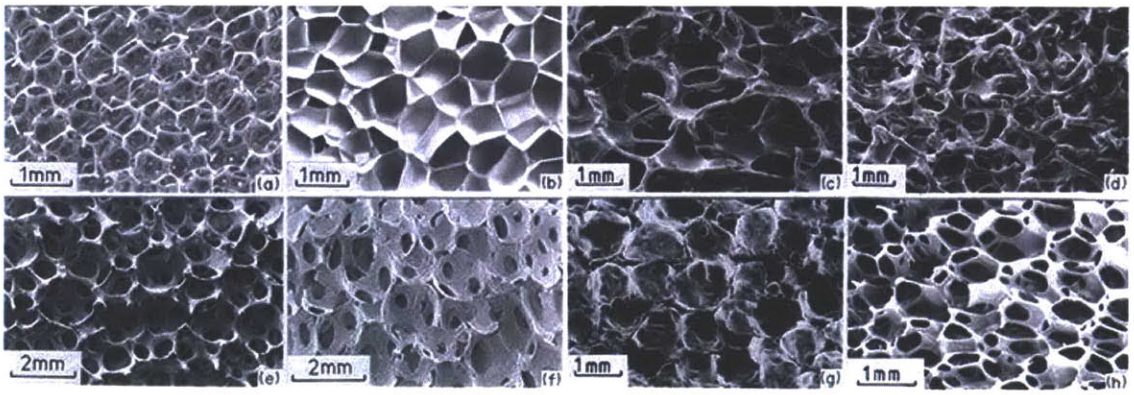


***Figure 2.3.*** *Examples of Randomly Filled Cellular Solids: (a) Open-cell polyurethane (b) closed-cell polyethylene (c) nickel (d) copper (e) zirconia (f) mullite (g) glass foams and (h) a polyether*

*foam with both open and closed cells (Courtesy of Gibson et al. 1997, Image retrieved from https://lornagibson.org/research).*

### 2.3.2. Properties of Cellular Solids

Most of the mechanical and thermal properties of cellular solids greatly depend on the shape, the topology of the cells, and its relative density rather than the size of the cells (Gibson et al. 1997). The relative density can be calculated as the following:

$$\varepsilon = relative\ density = \frac{\rho^*}{\rho_s} \qquad \text{(Eq. 2.1)}$$

where $\rho_s$ is the density of the bulk material used for the cellular wall, and $\rho^*$ is the density of the cellular material. Besides the relative density, the porosity is used instead as well to speculate the properties of cellular solids.

$$\phi = porosity = \frac{total\ void\ volume}{total\ volume\ of\ the\ foam} \qquad \text{(Eq. 2.2)}$$

In case of cellular solids with air in the cavity, as the weight of air, $w_{air}$, is negligible, the relative density can be expressed:

$$\varepsilon = \frac{\rho^*}{\rho_s} = \frac{\frac{w_{gyorid} + w_{air}}{V_{total}}}{\frac{w_{gyorid}}{V_{gyroid}}} = \frac{\frac{w_{gyorid}}{V_{total}}}{\frac{w_{gyorid}}{V_{gyroid}}} = \frac{V_{gyroid}}{V_{total}} = \frac{1 - V_{void}}{V_{total}} = 1 - \phi \qquad \text{(Eq. 2.3)}$$

The scaling relations for the mechanical properties and the thermal properties of cellular solids depend on the type of the cellular solids, the geometry of the cells and the topology of the cells. The relationships are derived from modeling and experimental data, and even though the relationship can be varied for certain type of cellular solids, the scaling relations for foam properties can be expressed as follows (Ashby 2000):

$$\frac{P^*}{P_s} = \alpha \left(\frac{\rho^*}{\rho_s}\right)^n \quad \text{(Eq. 2.4)}$$

where $P$ is a property, $\alpha$ a constant, and $n$ a fixed exponent. According to *Metal Foams: A Design Guide* by Ashby et al. the Young's modulus (GPa), $E$, and the thermal conductivity (W/m·K), $\lambda$, for open-cell foam can be approximated by the following equations:

$$E^* = (0.1 - 4)E_s \left(\frac{\rho^*}{\rho_s}\right)^2 \quad \text{(Eq. 2.5)}$$

$$\left(\frac{\rho^*}{\rho_s}\right)^{2.8} < \frac{\lambda^*}{\lambda_s} < \left(\frac{\rho^*}{\rho_s}\right)^{2.65} \quad \text{(Eq. 2.6)}$$

However, these equations are re-evaluated later before applied to the modeling or performance calculation in Chapter 4 and 5.

### 2.3.3. Advantages and Applications of Cellular Structures

Cellular solids are widely applied in various fields for their advantages: lightweight, thermal insulation, and structural strength. With their thermal insulation advantages, the products are varied from package filler to the insulation plates for rocket booster in the space shuttle. Also, many natural structurally strong materials are cellular solids, including wood and cancellous bone. More recently, the sandwich panels, cellular solid enclosed by two plates, are widely used in automobile industry and other similar design fields (Fig. 2.4). Accordingly, research on cellular solids is conducted more recently with the need for more in-depth knowledge for their structural behaviors. As one fact that most agree, when compared to a hollow section, the foam-filled tubes can resist higher load with less deflection (Fig. 2.5) (Seitzberger et al., 1997). This thesis aims to apply the structural benefits of the foam-filling section for curtain wall façade mullion design to increase the stiffness of the mullion without enlarging the profile. Also with the advantage of thermal insulation due to air (or another filling medium with low thermal conductivity), the suggested application is expected to reduce the thermal conductivity of the mullion.

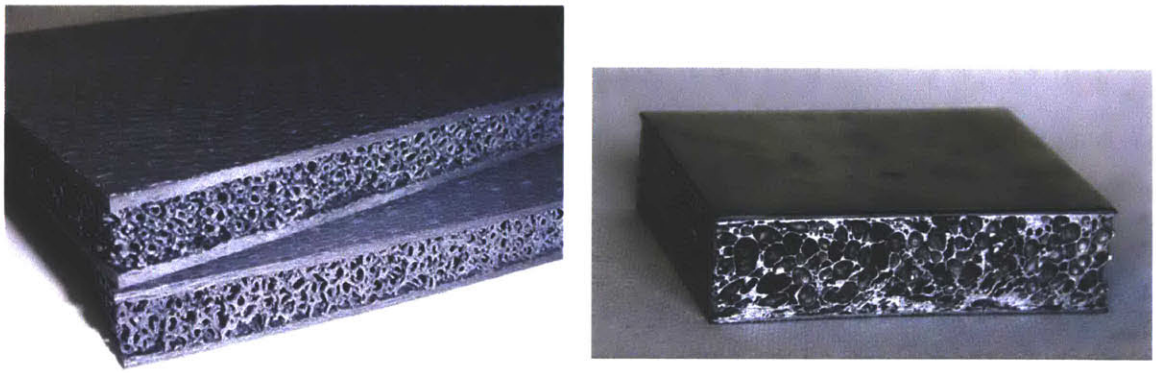

***Figure 2.4**: Examples of Cellular Structure in Applications: Ceramic Matrix Composite, or CMC (Left) (Courtesy of Engineering360), and Steel foam panel (Right) (Szyniszewski 2016).*

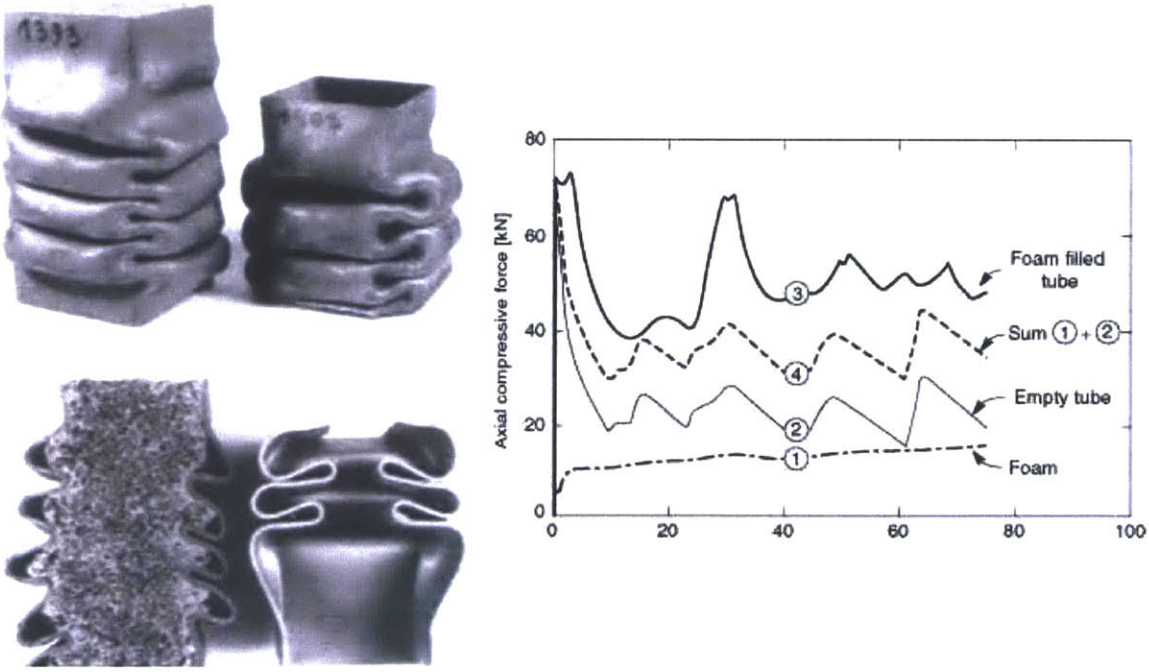


***Figure 2.5**: Sections through tubes with and without foam fillings, after partial crushing (Left); Load-deflection curves for a foam, a tube, and a foam-filled tube (Right) (Courtesy of Seitzberger et al., 1997)*

One can claim that the traditional curtain wall façade section already has an air gap that can act as an insulation layer within in the aluminum extrusion and therefore can ask why use cellular solids could be more beneficial to use. Based on thermodynamics, there are three fundamental ways of heat transfer: conduction, convection, and radiation. Free air by itself has a relatively low conductivity (R-2 for an 1/2 inch of "still" air) (Martin 2013); however, the transmitted heat can create a movement of the air molecules, and thus, the heat can be transmitted by the convection of the air the large cavity. In the meanwhile, the convection is insignificant for solids as the solid molecules hardly move around compared to the air molecules. In designed cellular solids, it is assumed that the air cavities are small enough to neglect the heat transfer by the convection in the air. By limiting the effects of the convection in the air with its small air cavities, the cellular solids is expected to use the air cavities as insulation bubbles with the low conductivity only of the air.

## 2.4. Gyroid

Among various types of cellular solids, the single-gyroid structure, also known as Schoen G surface, (called "gyroid" in this study), is chosen for its minimum surface area necessary to span a region of space (Fig. 2.6). Gyroid is triply periodic minimal surface that was first identified by Alan Schoen in 1970 (Schoen 1970). As the surface area is directly proportional to the rate of heat transfer, gyroid, with its definition of the minimal surface area, is expected to have an advantage in reducing the rate of heat transfer. In nature, the gyroid structure can be found from graphene assembly (Qin et al. 2016) to butterfly wings (Fig.2.7) (Winter et al. 2015). A close approximation to the gyroid is expressed by the following mathematical formula (Wohlgemuth et al. 2001, Scherer 2013 ):

$$F_{SG}(x,y,z) = t \qquad \text{(Eq. 2.7)}$$

$$\sin\left(\frac{2\pi}{L}x\right)\cos\left(\frac{2\pi}{L}y\right) + \sin\left(\frac{2\pi}{L}y\right)\cos\left(\frac{2\pi}{L}z\right) + \sin\left(\frac{2\pi}{L}z\right)\cos\left(\frac{2\pi}{L}x\right) = t \qquad \text{(Eq. 2.8)}$$

where $L$ is the cubic unit cell length and $t = 0$ for the minimal gyroid.

In this study, the following alternative equations are used for certain applications:

$$\sin(x)\cos(y) + \sin(y)\cos(z) + \sin(z)\cos(x) = 0 \qquad \text{(Eq. 2.9)}$$

$$\cos(x)\sin(y) + \cos(y)\sin(z) + \cos(z)\sin(x) = 0 \qquad \text{(Eq. 2.10)}$$

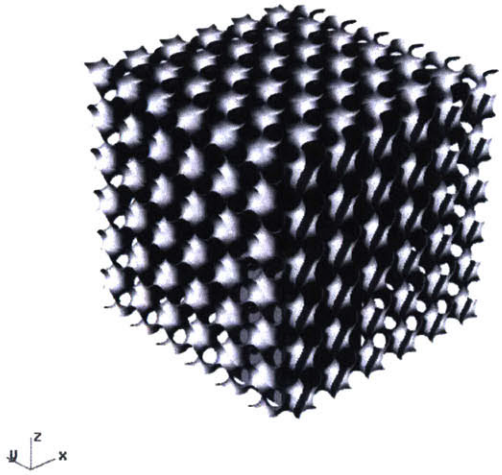


***Figure 2.6**: Sigle-Gyroid Surface in 3D*

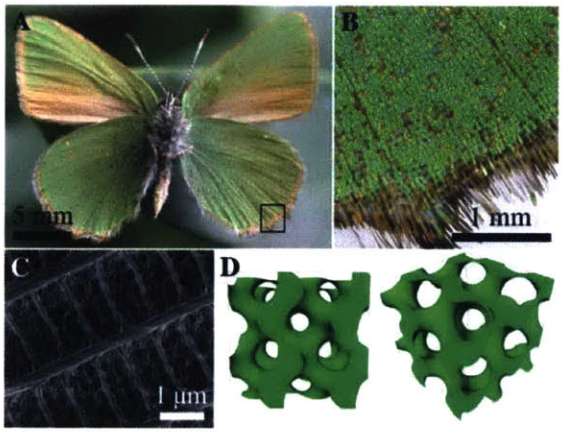


***Figure 2.7**: An Example of Gyroid Structure in Nature: Butterfly Wing in Micro-scale (Courtesy of Winter et al. 2015).*

The mathematical definition enables the digital modeling of the gyroid surface without a physical sample to be scanned and also allows for designers to control the density of the foam with precision. With the ability to control the density of the structure in micro scale, the designers can vary the density of the foam, which is directly related to the structural and thermal property of the foam. As for its category, the gyroid structure falls into open cell foam; for the cavity inside of the structure is connected and homogeneous, which can be beneficial to fill up the cavity with a fluid, if desired.

### 2.4.1. Need for New Cellular-Structure-based Mullion Design

This chapter has demonstrated the need for an innovative design solution to improve and optimize both structural and thermal performance of the curtain wall façade mullion. As a design solution, cellular structures are considered for their advantages in performance as insulation and stiffener. This thesis, in particular, selects gyroid for its definition of the minimum surface area, which is expected to yield less heat conduction through the surface area of the cells as compared to the other cellular structure. The next chapter will give a detailed methodology for modeling and materializing the gyroid structure in the application of the new mullion system design.

# Chapter 3. Modeling and Materialization

This chapter focuses on modeling gyroid structure digitally and producing physical structures to prepare the gyroid structure for the application in mullion design. The modeling process is mostly parameterized for a rapid modeling process, which is ideal for topology optimization process later on in this study.

## 3.1. Conceptual Overview

Gyroid by definition can be represented and modeled with its mathematical formula as mentioned in Chapter 2. However, due to its complex geometry, the resolution of digital models can affect not only the overall shape of the model but also the size of the model. For the compatibility and workability of the digital files, the resolution of the model is manipulated, and the mesh of the geometry requires refinements. In this chapter, gyroid structures are digitally modeled in three different ways: 1) using MATLAB (Mathworks 2015) and MeshLab, 2) using default components in Rhino 5 (Rhino)/Grasshopper (GH) (Robert McNeel & Associates 2015) and 3) using Millipede, a structural analysis and optimization GH plug-in, developed by Panagiotis Michalatos and Sawako Kaijima in 2014. Among the three, using Millipede component is the fastest way to model desired gyroid structures digitally. After a gyroid surface is generated, thickness is assigned to the surface by either offsetting the surface (in MeshLab or Rhino) (MeshLab 2014) or using a GH plug-in called Weaverbird, a topological mesh editor developed by Giulio Piacentino.

The refined digital models of gyroid structures are then used for 3D printing and simulations. For 3D printing, a Z Corporation (Z Corp.) 3D printer and a Stratasys 3D printer, Object 500, are used. The 3D printed models by Object 500 are later used for structural strength testing. Rather than the material choices for end-use materialization, this thesis focuses on topology design options to find comparative relationships between relative densities of the gyroid and their performance measures.

## 3.2. Digital Modeling

### 3.2.1. MATLAB Code and MeshLab

As for the initial modeling attempt, an edited portion of the script in MATLAB written by Zhao Qin (Qin 2016) is used to plot 3D points and triangulated mesh of a unit gyroid cell (Figure 3.1). The generated 3D points and triangulated meshes are then refined in MeshLab, an open source program for the processing and editing of unstructured 3D triangular meshes. The resulted surface is shown in Figure 3.2. The procedures are as follows and repeated if necessary:

1) The normal vectors for the point sets are computed first with "Neighbor num" as 10 and "Smooth Iteration" as 2.
2) Then, the surfaces are reconstructed with the ball-pivoting algorithm to smooth the generated surfaces.
3) To be prepared for 3D print, "Uniform Mesh Resampling" with "Clean Vertices" and "Absolute Distance" are used. The input values for the precision and the offset were initially set to "4" and "1" as for "world unit;" these values were incrementally modified for a "reasonably" well-defined gyroid structure. If the offset number is too high, the gyroid surface can be rough (Figure 3.3); otherwise, the gyroid surface has a very thin surface with a relatively large number of vertices.

In the mesh refining process, the regeneration of triangulated mesh can be time-consuming and require a computer that is capable of a heavy computation with high-quality graphic cards. Thus, some compromise in resolution is needed for the post-digital modeling process. The generated mesh with a thickness from MeshLab is imported into Rhino and saved as .stl files for 3D printing.

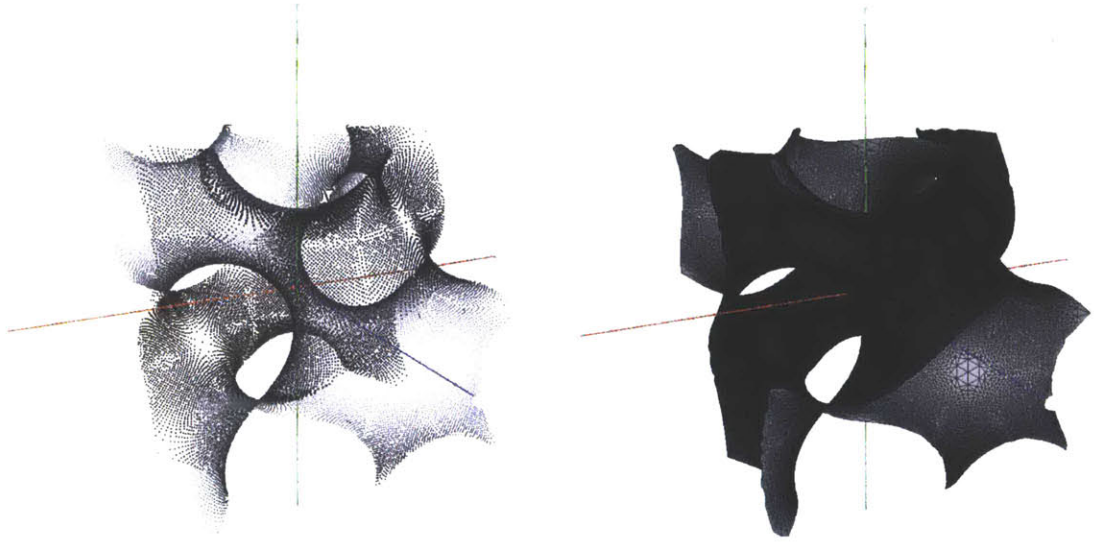

***Figure 3.1**: 3D points (Left) and triangulated mesh of a unit gyroid cell surface (Right)*

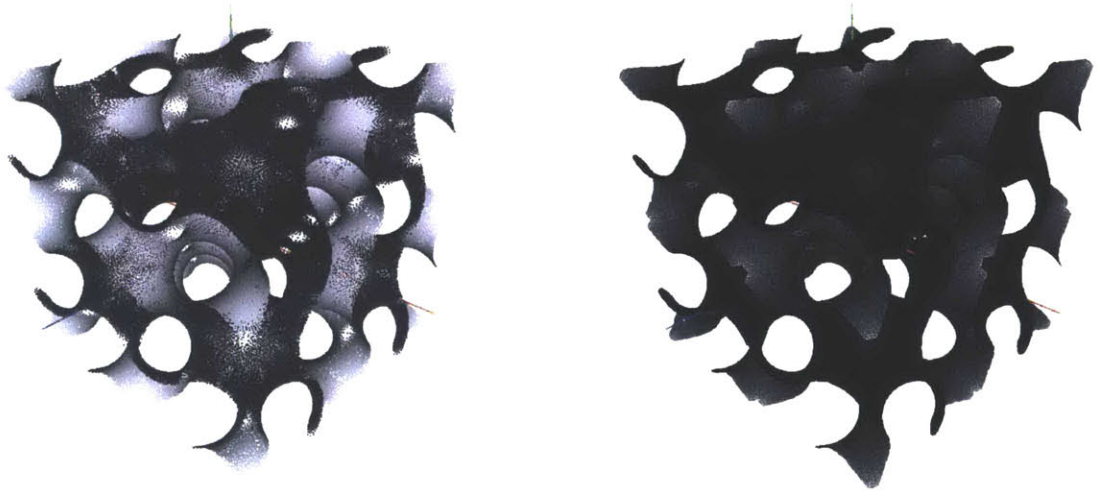

***Figure 3.2**: 3D points (Left) and gyroid surface with multiple periods (Right)*

MeshLab is powerful in refining a complex mesh with a suitable number of mesh faces and nodes; however, the "Uniform Mesh Resampling" process can be computationally intensive for the complex geometry, and the output mesh could have the large number of vertices and faces. Also, if one tries to copy and paste a unit cell next to each other to produce a gyroid with more units, there could be a crack or missing mesh segments along the pasted face (Figure 3.3). These

holes in the mesh can be difficult to fill in MeshLab for its relative size to the true cavities in gyroid and for the sign number of mesh faces to be processed. Thus, for this study, another modeling method is sought to be time-efficient.

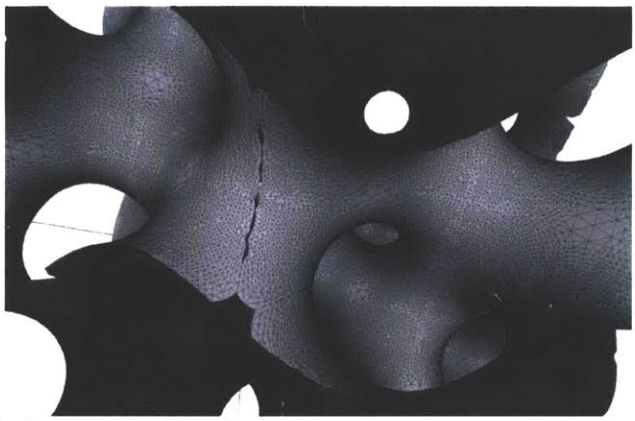

***Figure 3.3**:Errors with disconnected mesh surfaces*

### 3.2.2. Approximated Surfaces in Rhino/Grasshopper

With the need for a rapid digital modeling method, an approximated gyroid surface is modeled using their default components in Rhino and Grasshopper. The approximation was graphically made by the following procedures, which are modified from Seth Moczydlowski's approach (Moczydlowski 2015):

(1) Create a cube for a frame.

(2) Draw sinusoidal periodic curves that on each face of the cube.

(3) Isolate a repeating unit within the cube (1/8 of the cube). (Figure 3.4.A)

(4) Create a line segment that is perpendicular to the plane that each curve on the face of the cube sits in, at its midpoints.

(5) Connect the line segments that are facing each other and draw a curve using "Blend Curve," and "ReBuild Curve." (Here, the lines must meet at the center of the repeating unit, and the number of control points largely influences how surfaces are defined. The ideal number that is used in this study is "5" for the number of counts for "ReBuild Curve.")

(6) Using the drawn lines, draw sub-surfaces (total of 6) and group the surfaces as one unit gyroid surface. (Figure 3.4.B and C)

(7) Repeat and rotate the unit gyroid surface and place accordingly to form multiple units of gyroid surface. (Figure 3.4.D)

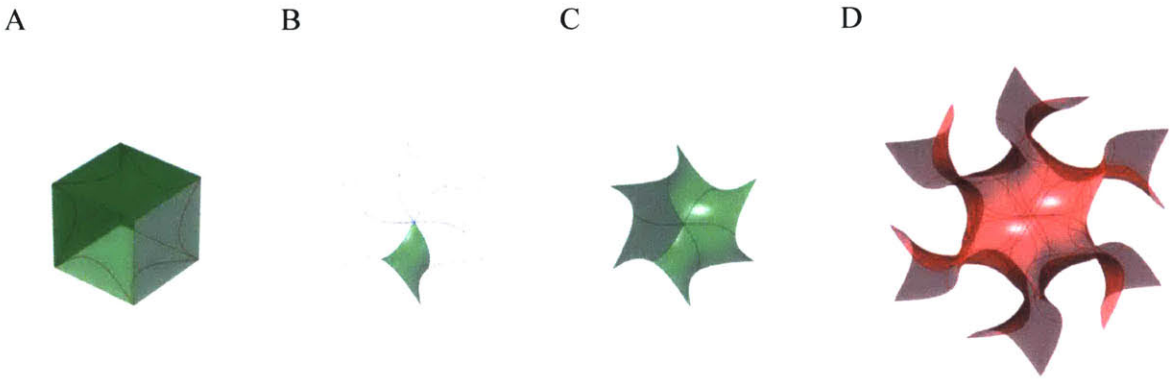


***Figure 3.4**: Progression of defining approximated gyroid surfaces*

To assign a volume from the generated surfaces in (7), one can do either of the following two ways: a) offsetting of the surfaces and adding the edge surfaces to make a closed volume or b) refining the thickened mesh using "Weaverbird's Mesh Thicken." The (b) method can be faster; however, the 2-pi unit surfaces (defined as the code above) have to be "thickened" prior to "copying and arraying" to occupy the desired volume. Otherwise, the code does not run, for the "Weaverbird's Mesh Thicken" operates with a closed solid mesh while the 2-pi unit surface defined above is defined as an open mesh. Moreover, the result of (b) can be very crude without refining as showing in Figure 3.5.

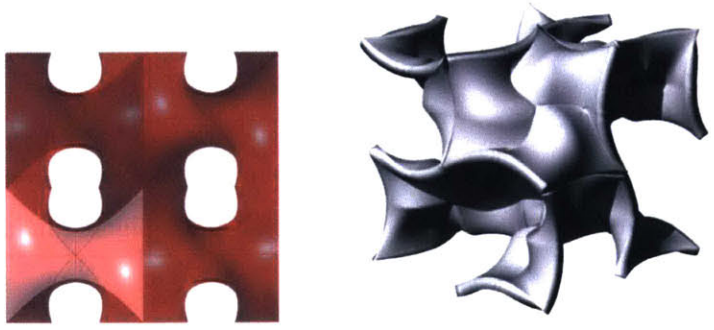

***Figure 3.5**: Errors in the Approximated Method*

Moczydlowski's approach utilized only modeling components in Rhino, but to have the ability to modify the surface model more efficiently, the generated surfaces are defined and parameterized in Grasshopper. This method of modeling gyorid has an advantage of fast modeling due to the relatively small number of mesh in the digital structure; the unit surface is modeled with only six sub-surfaces. In the meanwhile, this method depicts an approximation of the true gyroid surface; thus, the structure behavior and properties calculated or achieved using the models generated by this approach could have potential errors. Nonetheless, this method can be useful to produce gyroid-like digital models rapidly, if the unit cell is repeated for a number of times with a small size of cavities.

### 3.2.3. Modeling with Millipede in Rhino/Grasshopper

As the previous modeling approach required improvement in the quality and speed of digital modeling gyroid structures in Rhino/Grasshopper environment, another grasshopper script was written with the components from various Grasshopper plug-ins, such as Millipede and Weaverbird as the backbone components for generating the gyroid surface. One of the major components in the code is a component called "Iso-Surface" defined from Grasshopper plug-in, "Millipede." This method is a more refined version of the method described in (ii) in that it uses a mathematical equation of gyroid to generate a mesh with a user-defined resolution. The summary of the code is described as follows:

(1) Create x,y,z points using "Evaluate," with an input resolution and gyroid equation as the following:

$$\cos(x)\sin(y) + \cos(y)\sin(z) + \cos(z)\sin(x) = 0 \qquad \text{(Eq. 2.10)}$$

(2) Define a target volume.

(3) Use the calculated points for "Iso Surface" from Milipede to generate a surface mesh.

(4) Use the Weaverbird's components to refine mesh and assign a thickness to the mesh.

When manipulating the generated surfaces from this method, one needs to be careful in post-processing as the generated surfaces are defined as "mesh" while most of the GH component for intersection requires the input as "Brep." Even with "Mesh Intersection" or "Mesh Split," errors

can occur. Thus, when "Mesh Intersection" yields an error, the mesh needs to be converted to "Brep;" which can be done with a commend "Mesh2Brep" in Rhino, not in Grasshopper.

The advantage of this method is that, compared to the previous method in 3.2.2., the generated surface is smoother as the points are derived from the mathematical definition of gyroid. Also, the various GH plug-in components aid to perform calculations and visualization interactively in the Rhino environment. For its rapid production of reasonably accurate digital models, this method is used for the following computational simulations and final product modeling.

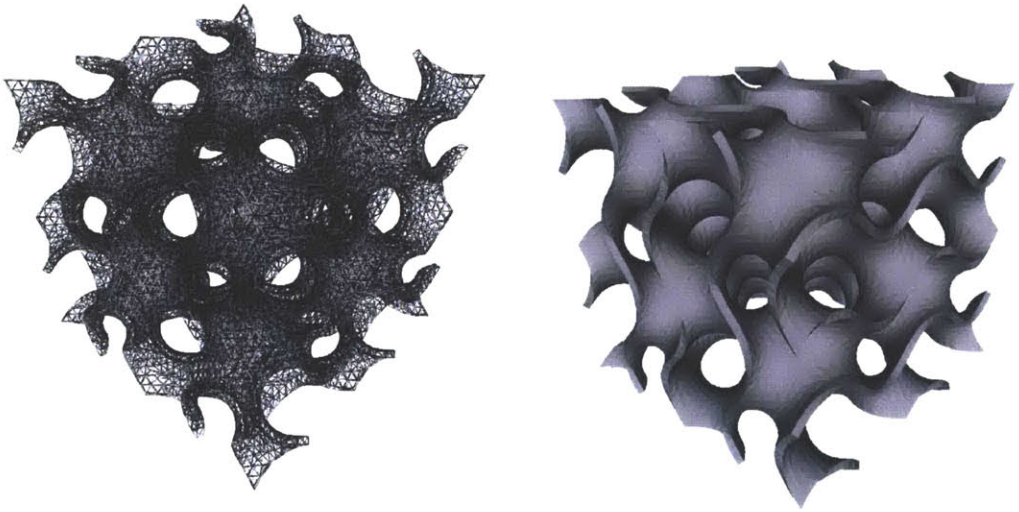

***Figure 3.6**: Gyroid generated in GH with Millipede and Weaverbird components.*

## 3.3. Materialization via 3D Printing

### 3.3.1. Conceptual Overview

The currently available method to produce a gyroid structure is with 3D printing due to its complex geometry. In this study, two different 3D printers, one from by Z Corporation (ZCorp) or 3D Systems and the other from Stratasys, are used to print gyroid structures for not only visualization but also for the experiments conducted in Chapter 4. Each printer utilizes different printing techniques and materials; thus, printed models are used differently for their speculated properties. For the experiment carried out in Chapter 4, the printed models by ZCorp are initially assigned for the heat flow experiment; and the printed models by Stratasys' printer for the compression/tension test.

### 3.3.2. ZCorp 3D Printer

#### 3.3.2.1. Material and Method

The ZCorp Printer uses standard inkjet printing technology to create parts layer-by-layer by depositing a liquid binder onto thin layers of powder. The properties of the white powder used in the ZCorp printer are speculated to be similar to that of sand or ceramics, as with the lack of product information. Before printing, a gyroid surface is first modeled by the method described in 3.2.1, scaled to be fit in 10 cm by 10 cm by 10 cm cube, and converted to .stl file as shown in Fig. 3.7. Then, the .stl file is sent to print the model as shown in Fig. 3.8.

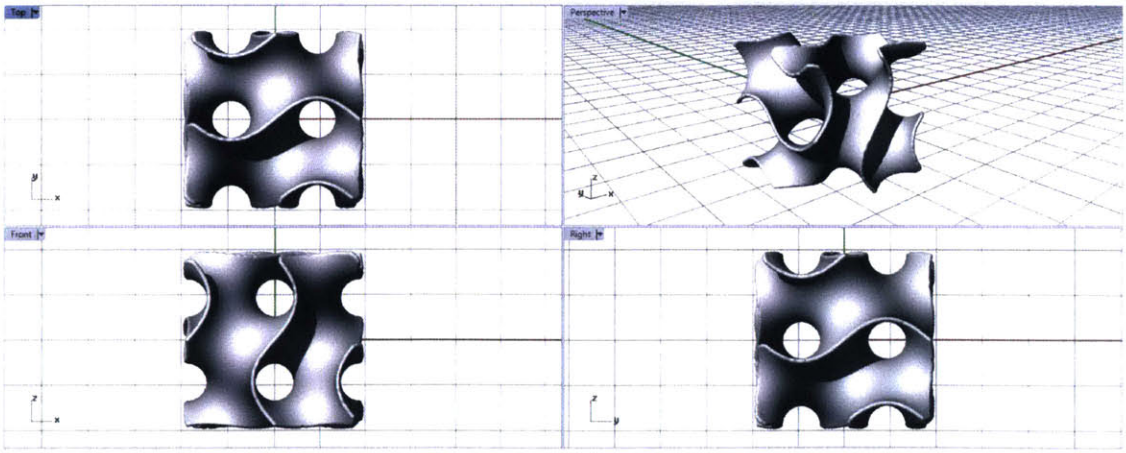


***Figure 3.7**: Rendered views of the digital model used for ZCorp printing*

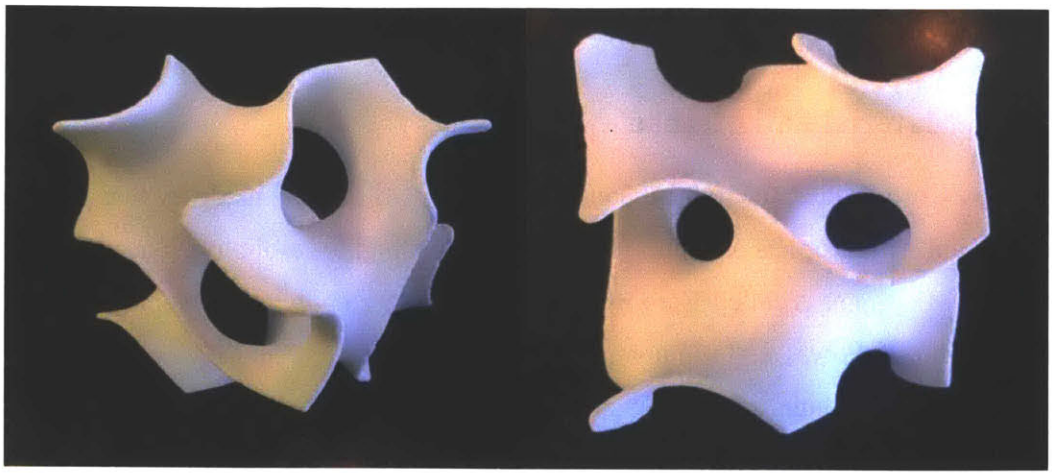

***Figure 3.8**: Photos of the gyroid printed by ZCorp*

### 3.3.2.2. Pros and Cons

The ZCorp Print can be useful for rapid printing and visualization. As compared with the other printer, the ZCorp Print requires a minimum post-printing process: to remove the excess powder with air blower and brushes. However, if the printed model is desired to have higher structural strength, additional solidifying processes are needed: soaking the printed model in a solution with resin and drying. Without the solidification process, the printed model is brittle and can have weak bondage in between the layers (Fig 3.9).

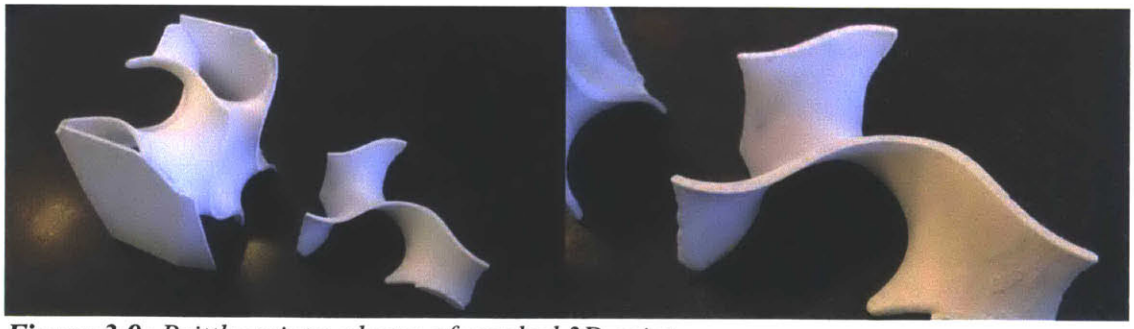

***Figure 3.9**: Brittle prints: photos of cracked 3D prints.*

### 3.3.3. Object 500 by Stratasys

#### 3.3.3.1. Material and Method

Similar to the ZCorp Printer, the multi-material 3D printer Object 500, made by Stratasys, prints layer by layer but with droplets of liquid photopolymer in a higher resolution. The material used with Stratasys' 3D printer is called Veromagenta, a pink-colored polymer. The properties of the Veromagenta are as follows: $\rho_s$=1175 mg/cm3, $E_S$=2.45 GPa and $\sigma_{Ts}$=50 MPa corresponding to the density, Young's modulus and tensile strength of the bulk material properties (Stratasys 2016). The printed models with a broad range of relative densities are shown in Fig. 3.10: the printed models have volumes of either $1.5\times1.5\times1.5$ inch$^3$ or $1.0\times1.0\times1.0$ inch$^3$ and with various thicknesses.

#### 3.3.3.2. Pros and Cons

Stratasys's 3D printer is useful when printing a complex geometry in polymer material with a higher resolution. As shown in the Fig. 3.10, the printed models have smooth and intact surfaces. However, the post-printing process can be labor-intensive in that the supporting wax has to be removed; for the models with thinner gyroid surfaces, the cracks can be easily made when removing wax (Fig. 3.11). Although the Stratasys' model require additional processes, the printed models by the Stratasys' printer exhibit workable structural strengths, which allows the printed models to be tested under compression/tension loads.

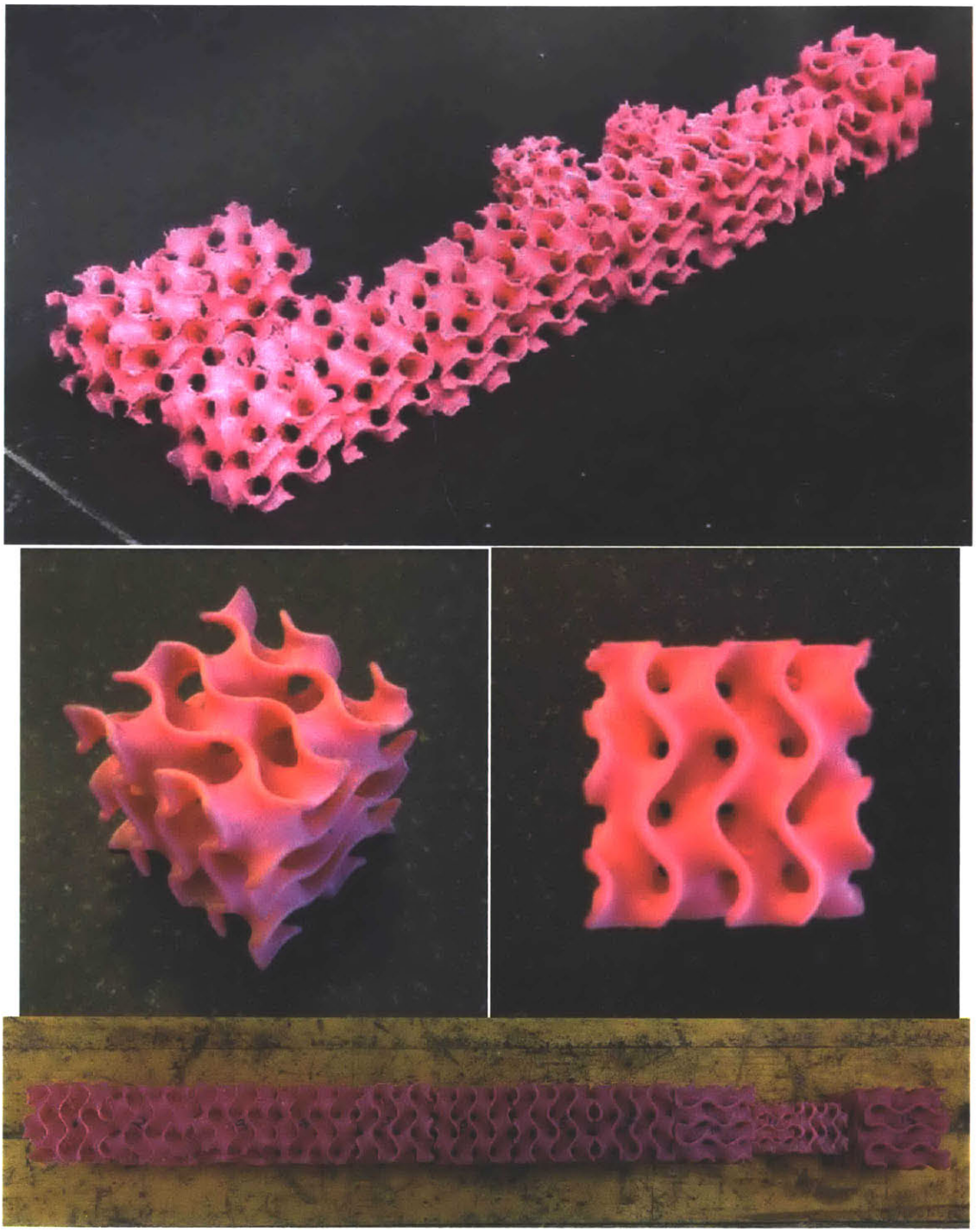

***Figure 3.10**: Photos of gyroids 3D-printed by Object 500 made by Stratasys.*

***Figure 3.8**: Issues with post-printing process required for the 3D printed models by Stratasys's 3D printer: Wax to be removed (Left) and cracks made for prints with thinner gyroid surface during cleaning process (Right)*

## 3.4. Summary

Various modeling methods were explored in this chapter, and as for a rapid modeling method, a GH script with Millipede and Weaverbird components is selected for general gyroid modeling, and especially for the optimization study. Meanwhile, the printed gyroids models by Object 500 are used for mechanical experiments for its durability as compared to the models printed by ZCorp Printer.

# Chapter 4. Assessment via Physical Experiments and Simulation

The purpose of this chapter is to study the structural behavior and thermal properties of various densities of gyroid structure. The scaling relations of the structural properties and thermal properties are obtained in this chapter for the optimization study in Chapter 5.

## 4.1. Conceptual Overview

To achieve the structural performance, mechanical testing is performed using the 3D printed gyroid models in the Civil and Environmental Engineering Laboratory at MIT. The compression and tension test were conducted to find the Young's moduli of different densities of 3D printed gyroid. The experimental results are then compared with the theoretical values using an equation for open-cell structures (Gibson et al. 1997) and with other experimental values for graphene, which has a gyroid structure (Qin et al. 2016). Secondly, the relationship between the thermal properties and the relative densities of gyroid is attempted to be obtained by heat transfer simulation using Abaqus and heat flow experiment using the Heat Flow Meter by Netzch.

## 4.2. Theoretical Structural Properties of Gyroid

Mechanical properties of cellular structures as discussed in Chapter 2 can be calculated using the relative density of the cellular structure and its shape. As a gyroid structure is treated as an open cell structure in this study, the equations of an open cell structure are used initially to obtain theoretical values for Young's modulus, $E$, of gyroids with different relative densities.

According to Ashy and Gibson, the Young's modulus for open cell foam can be calculated using Eq. 4.1 (Gibson et al. 1997).

$$\frac{E^*}{E_s} = C_1 \left(\frac{\rho^*}{\rho_s}\right)^2 \qquad \text{(Eq. 4.1)}$$

where $C_1$ is a constant value that can be derived by experimental data: $C_1 = 1$ for a typical open cell foam. However, this equation is only used as a reference since the exponential value in Eq. 4.1 for the relative density, given as 2, can vary for the shape of the cellular structure.

When finding the relationship based on the experimental data achieved in this chapter, the value for n is sought while assuming $\alpha = 1$ in Eq. 4.2 which is the general scaling relation for cellular structure (Ashby 2000):

$$\frac{P^*}{P_s} = \alpha \left(\frac{\rho^*}{\rho_s}\right)^n \qquad \text{(Eq. 4.2)}$$

## 4.3. Mechanical Testing

### 4.3.1. Methodology

Before the testing, each of the 3D printed models (Fig. 3.10) was weighed first to calculate its relative density. Then, the tensile tests and the compression tests have been carried out at room temperature with a standard tensile testing machine (MTS Corporation, Eden Prairie, Minnesota, USA). In each of the tensile tests, the 3D printed model is attached to two T-shape aluminium substrates by approximately a 0.2-in-high pool of epoxy glue. The two T-shape aluminium substrates were fixed to the top and bottom cross heads, which moved at a constant rate of 0.01 mm/s displacement. For each of the compressive tests, the 3D printed models are compressed by the two cross heads, which have large flat surfaces. The upper cross-head was held by a force transducer where the reaction force was measured. The cross-head displacement is measured using a linear voltage displacement transducer mounted inside the actuator. The total force and displacement of the substrate were scanned with 1 Hz and saved to the connected data collector. The test subjects were regularly checked for detachment or misalignment. Figure 4.1 illustrates the specimens under both tensile tests and compression tests.

A

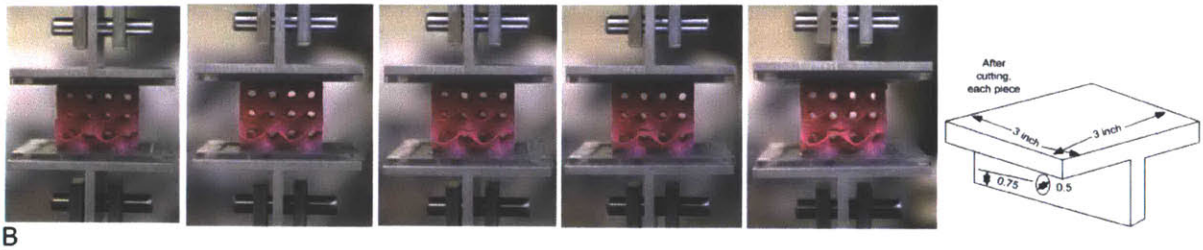


B

***Figure 4.1**: Photos of tensile tests with a schematic drawing of the T-shape aluminum substrate glued to the specimens (A) and compression tests (B) (Courtesy of Qin et al. 2016).*

The obtained experimental data from the mechanical testing was used to calculate the Young's modulus, the tensile strength, and the compressive strength of each model. The calculated structural properties were then compared to other experimental values for a graphene, which exhibits a gyroid structure (Qin et al. 2016), to obtain scaling relations.

### 4.3.2. Mechanical Test Results

The tested results for the tensile test and compression test are plotted in the stress-strain curves as shown in the Figure 4.2. As expected, the relative density increases; both compressive and tensile strengths increase for gyroid. Table 4.1 shows the numerical values for the calculated relative densities, the Young's moduli, the tensile strengths, and the compressive strengths of the tested models. The graph in Fig. 4.3 illustrates the relationship between the relative Young's modulus and the relative density; similarly, the relationship between the relative tensile strength and the relative density is described in the Fig. 4.4. The obtained equations are:

$$\frac{E^*}{E_s} = 2.09\left(\frac{\rho^*}{\rho_s}\right)^{2.82} \qquad \text{(Eq. 4.3)}$$

$$\frac{\sigma_T}{\sigma_{Ts}} = 0.30\left(\frac{\rho}{\rho_s}\right)^{1.6} \qquad \text{(Eq. 4.4)}$$

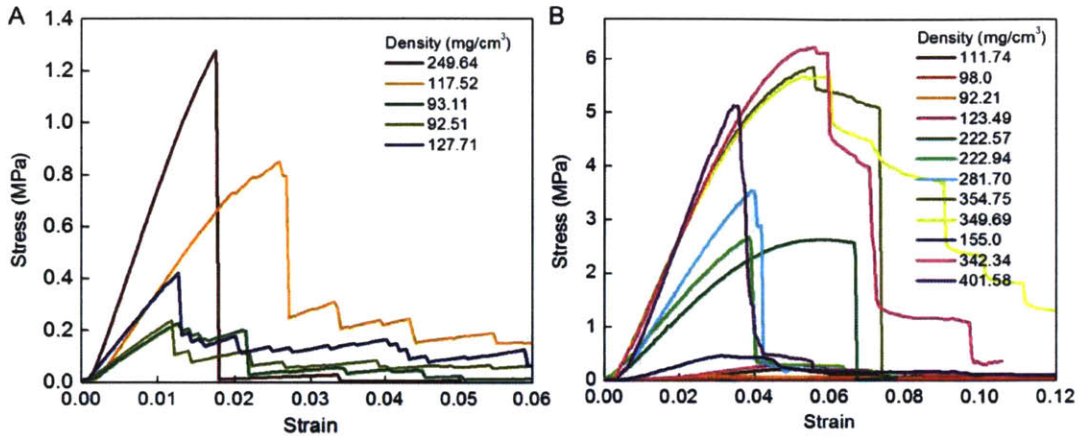


***Figure 4.2**: Stress-Strain curves of 3D printed gyroid samples in A tensile and B compressive tests (Courtesy of Qin et al. 2016).*

| Tensile tests | | | |
|---|---|---|---|
| **Model #** | **$\rho$ (mg/cm$^3$)** | ***E* (MPa)** | **$\sigma_T$ (MPa)** |
| **1** | 249.64 | 85.58 | 1.28 |
| **2** | 117.53 | 43.35 | 0.85 |
| **3** | 93.12 | 20.52 | 0.23 |
| **4** | 92.52 | 21.83 | 0.24 |
| **5** | 127.71 | 36.60 | 0.42 |
| **Compression tests** | | | |
| **Model #** | **$\rho$ (mg/cm$^3$)** | ***E* (MPa)** | **$\sigma_T$ (MPa)** |
| **1** | 111.74 | 7.03 | 0.21 |
| **2** | 98.0 | 2.98 | 0.07 |
| **3** | 92.21 | 4.08 | 0.09 |
| **4** | 123.49 | 9.40 | 0.29 |
| **5** | 222.58 | 68.23 | 2.63 |
| **6** | 222.94 | 75.15 | 2.67 |
| **7** | 281.70 | 109.39 | 3.55 |
| **8** | 354.75 | 151.67 | 5.86 |
| **9** | 349.69 | 149.95 | 5.69 |
| **10** | 155.00 | 19.04 | 0.46 |
| **11** | 342.34 | 155.02 | 6.24 |
| **12** | 401.58 | 184.94 | 5.13 |

***Table 4.1**: Summary of the structural properties of 3D printed gyroid structures with various densities. The mechanical properties for the bulk polymer material used in 3D printings are: $\rho_s$=1175 mg/cm$^3$, $E_S$=2.45 GPa and $\sigma_{Ts}$=50 MPa corresponds to the density, Young's modulus and tensile strength (Courtesy of Qin et al. 2016).*

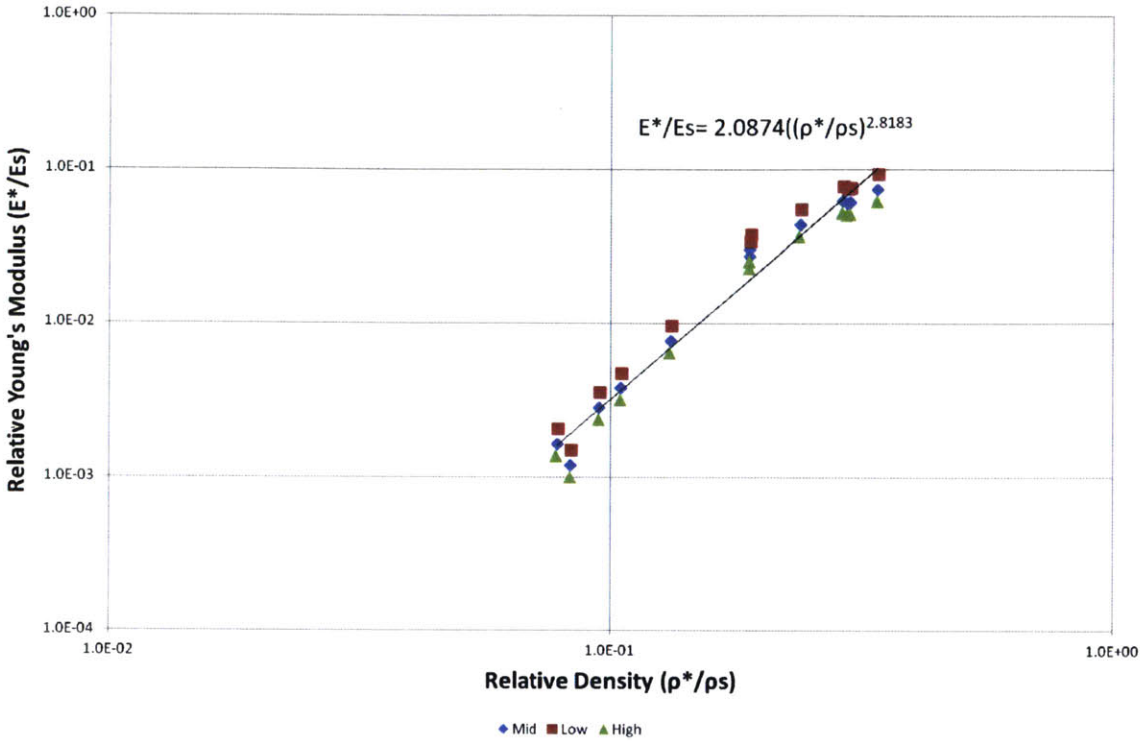


***Figure 4.3**: Relative Young's Modulus vs. Relative Density*

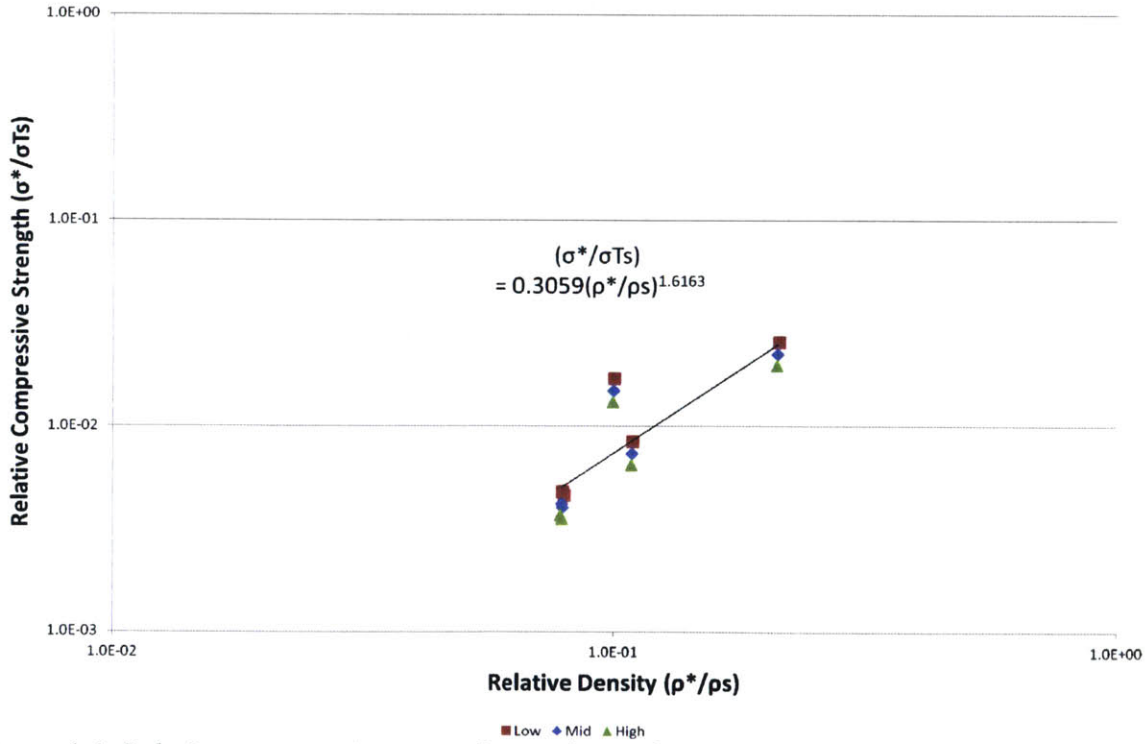


***Figure 4.4**: Relative compressive strength vs. relative density.*

### 4.3.3. Mechanics of Gyroid

The test results showed that the strength of the gyroid structure depends on its density, and the trend is similar to that of the open cell structure but with a higher exponential value for the relative density term in the scaling relations. The results are compared with the other experimental data for gyroid structure to obtain more reliable equation for gyroid structures (Fig. 4.5), and the equations for the fitted curves are (Courtesy of Qin et al. 2016):

$$\frac{E}{E_s} = \left(\frac{\rho}{\rho_s}\right)^{2.73\pm0.09} \quad \text{(Eq. 4.5)}$$

$$\frac{\sigma_T}{\sigma_{Ts}} = \left(\frac{\rho}{\rho_s}\right)^{2.01\pm0.05} \quad \text{(Eq. 4.6)}$$

$$\frac{\sigma_C}{E_s} = \left(\frac{\rho}{\rho_s}\right)^{3.01\pm0.01} \quad \text{(Eq. 4.7)}$$

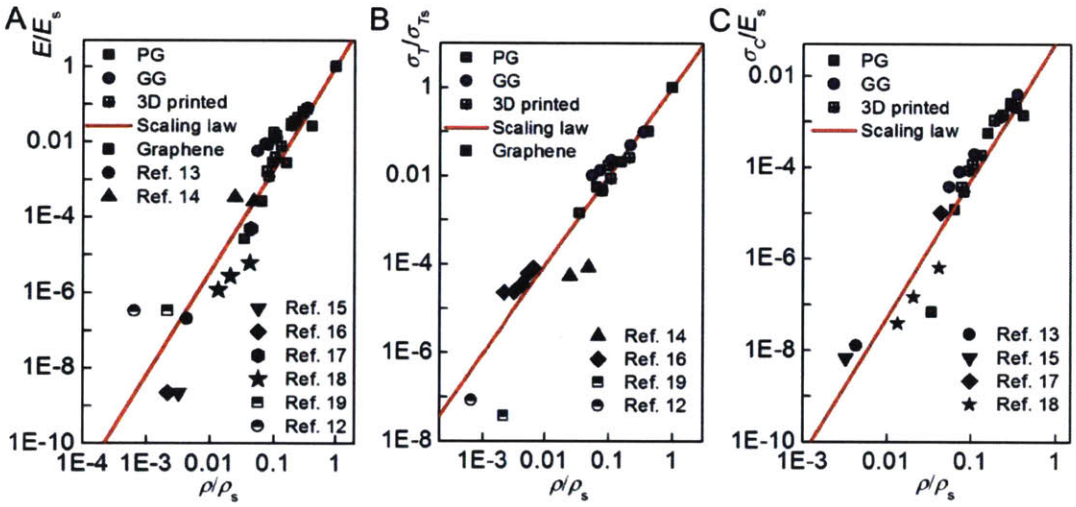


***Figure 4.5**: The normalized Young's modulus (A), tensile strength (B) and compressive strength (C) of the 3D graphene assembly as a function of its mass density (Courtesy of Qin et al. 2016).*

The exponential value, $n$, obtained for gyroid in this experiment was 2.73, slightly larger than 2 as in Eq. 4.1, which is given for general open cell structures by Ashy and Gibson. Nonetheless, the resulted equation Eq. 4.5 shows that the experimental results obtained in this thesis follow the scaling relation as the other cellular structures: in Eq. 4.2, $n = 2.73$.

## 4.4. Theoretical Thermal Properties of Gyroid

As the gyroid structure is categorized as an open cell structure, the conductivity of a composite gyroid structure can be obtained using the equations for open cell structures. Several theoretical equations exist as to calculate thermal conductivity for open cell structures (Kamiuto 2008). Among various equations, the following equations by Schuetz and Glicksman are recommended by Kamiuto for open cell structures for its best correlation with experimental data when compared (Kamiuto 2008):

$$\frac{k_{eff,c}}{k_f} = \phi + \frac{1}{3}(1-\phi)(\frac{k_s}{k_f}) \quad \text{(Eq. 4.8)}$$

$$k_{cf} = \phi k_f \quad \text{(Eq. 4.9)}$$

$$k_{cs} = \frac{(1-\phi)k_s}{3} \quad \text{(Eq. 4.10)}$$

Thus,

$$k_{eff,c} = \phi k_f + \frac{1}{3}(1-\phi)k_s \quad \text{(Eq. 4.11)}$$

## 4.5. Heat Transfer Simulation using Abaqus

### 4.5.1. Assumptions

To conduct a heat transfer simulation with a simplified model, the following assumptions are made:

- All the components are modeled as rigid solid bodies with no chemical interaction.
- Steady-state heat transfer is considered, and the set temperatures used are based on the location in Boston, MA area; the interior temperature to be 21°C and the exterior temperatures to be -37 °C, the lowest, and 42 °C, the highest.
- The air inside of the section is assumed to be static.
- Convection and radiation effects are negligible.

### 4.5.2. Abaqus Model

The model used for the analysis is illustrated in the 2D-diagram in Fig. 4.6: the actual model used in the analysis is in 3D. The gyroid surfaces with a thickness, and the captured air are in between the two metal plates. The heat flows in the z-direction in the diagram, and the sides are set to be in adiabatic condition. The length of gyroid structure, $L_z$, is designed to be increased to check the effects of the depth on the resulted thermal conductivity of the entire structure. And the relative density of the gyroid is also designed to be varied to find the scaling relation of the thermal property of gyroid. As the experiment continued, the variation is compromised for the capability, and the first model attempted for the analysis was the unit gyroid cell (or with 1pi for the frequency period gyroid), with an intention to perform a simplified calculation based on the thermal resistance network concept.

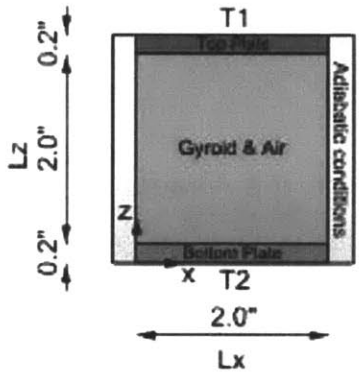


***Figure 4.6**: 2D diagram of the Abaqus model*

### 4.5.3. Preparing the Input Model in Rhino/Grasshopper

As to prepare for the simulation in Abaqus, the gyroid surface is carefully modeled with additional refining procedures, and five different volumes are defined before importing to Abaqus: the top plate, the bottom plate, the air above the gyroid, below the gyroid, and the gyroid structure. As the Weaverbird's "Mesh thicken" component produces a "thickened" mesh that slightly extends the boundary cube, the mesh requires trimming; however, the difference volume outside of the boundary cube is often too small for trimming in Rhino/Grasshopper. Thus, additional procedures are needed, which starts by "baking" the gyroid surface mesh generated from Grasshopper script as described in Chapter 3. To reduce errors in meshing, a larger surface mesh is generated, and after baking, the mesh is offset with a desired thickness,

0.1in. Then, the surface meshes are converted to Brep from Mesh with a commend "Mesh2Brep" in Rhino, not in Grasshopper. This conversion allows the surface mesh to be trimmed and split with boundary surfaces, in this case, the surfaces of a cube. Then, the trimmed gyroid surfaces and split portions of boundary surfaces are used to define two volumes of the surrounding air and that of gyroid (Figure 4.7). Moreover, the resolution of the mesh needs to be relatively low in order to avoid error and a heavy computation in Abaqus.

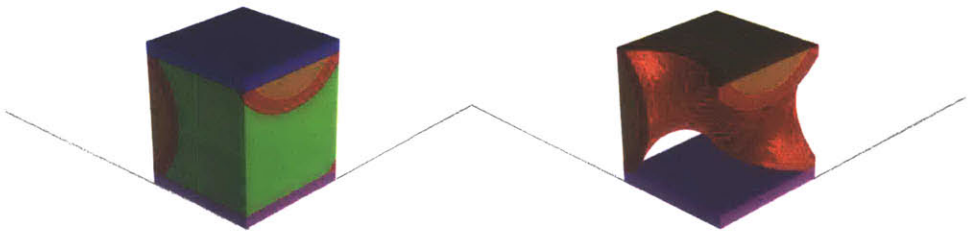

***Figure 4.7**: 3D view of the model used in Abaqus analysis: the air above the gyroid (Orange), the air below the gyroid (Green), the unit gyroid (Red), the top plate (Blue), the bottom plate (Magenta).*

### 4.5.4. Modeling in Abaqus

In modeling a composite gyroid structure in Abaqus, the meshing process and defining constraints are critical in that the imported volumes from Rhino require meshing, even if the volumes are defined with mesh surfaces. For mesh control, tetra element and Quad element are used instead of linear for tetra element (Fig. 4.8). When defining constraints, "adjust the initial nodes" option is unchecked to minimize the error due to complicated mesh. Instead of interaction, constraints with "Surface to surface" discretization method and "Tie rotational DOfs if applicable" option (or tie-constraints) are used for contact surfaces.

As for the material properties, the gyroid is modeled with the properties of cellular glass since cellular glass has a high thermal resistance, which value is in between thermal resistance of air and that of aluminum. Temperatures used in the analysis are: 21°C as the ideal indoor temperature, 42°C as the typical highest temperature in Boston, MA, -37°C as the typical lowest temperature in Boston, MA. In the first test model, T1 is set to be 21°C and T2 to -37°C. And all the volumes are models as solid, as the convection and radiation effects are ignored.

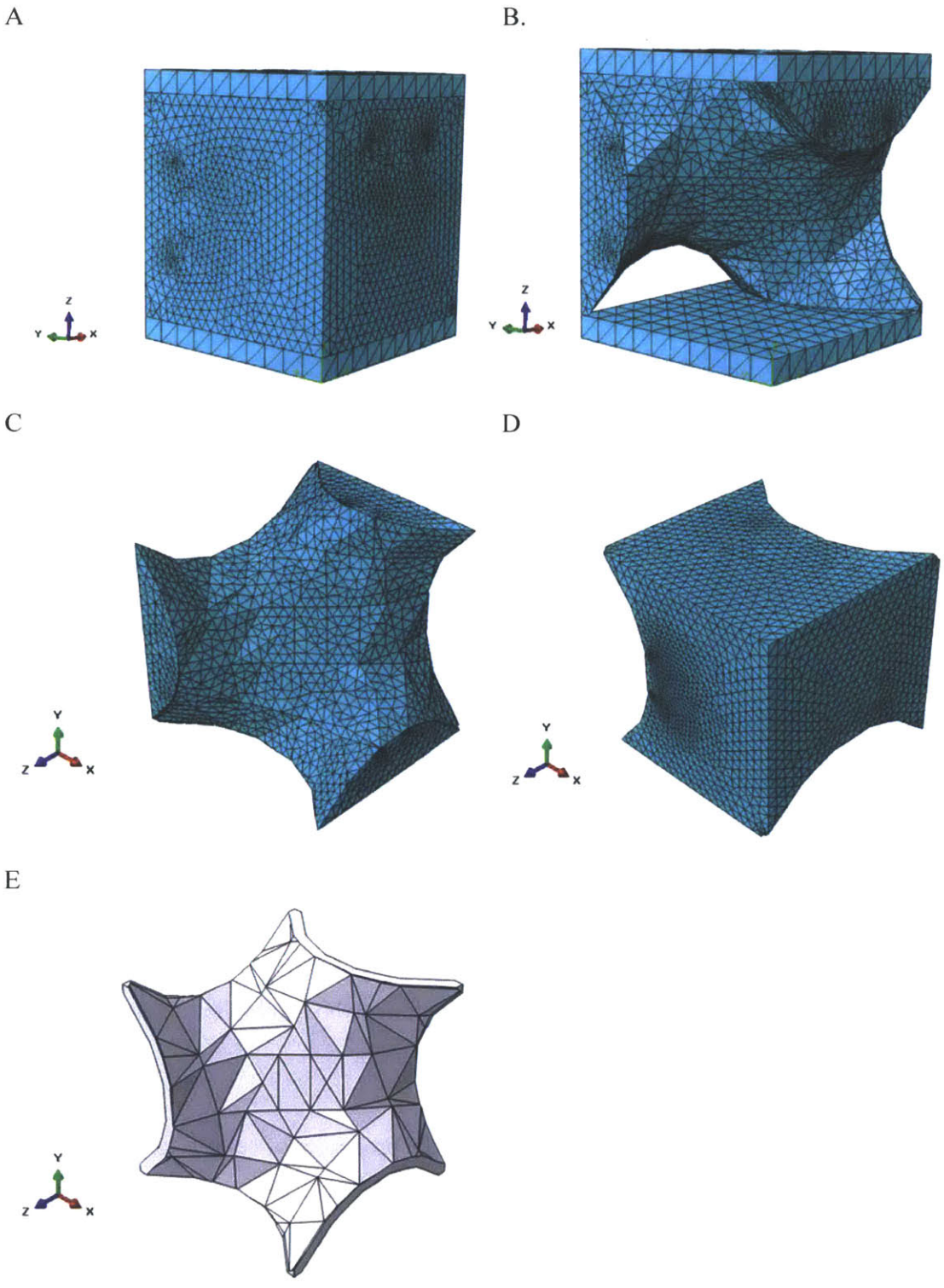


***Figure 4.8**: Meshed components in the model used in Abaqus analysis: 3D assembly (A), 3D assembly with the bottom air hidden (B), the bottom air alone (C), the top air alone (D), the gyroid alone (E).*

### 4.5.5. Post-analysis Process in Abaqus

As the Abaqus does not provide the output that conveniently shows the thermal resistance or thermal conductivity of the entire structure, the post-analysis process is designed to calculate the thermal resistance of the composite model, which accounts both the gyroid and the air in the cavity. Based on the basics of thermal dynamics,

$$\frac{|T_2 - T_1|}{Q} = R_{th} \quad \text{(Eq. 4.12)}$$

where $Q$ is the heat flux throughout the model in Watts, and $R_{th}$ is the thermal resistance in °C/W. The thermal resistance can be also expressed in:

$$R_{th} = \frac{l}{k_{eff}A} = \frac{l_1}{k_{eff}l_2 w} \quad \text{(Eq. 4.13)}$$

where $k_{eff}$ is the effective thermal conductivity; $l_1$, the length of the model in the direction of the heat flow; $l_2$, the length of the model perpendicular to the direction the hear flow; and w, another length of the model perpendicular to the direction the hear flow or the width of the surface area perpendicular to the direction of the heat flow.

Since $R_{th}$ and $k_{eff}$ are the desired values, the equations above can be rearranged as:

$$R_{th} = \frac{|T_2 - T_1|}{Q} \quad \text{(Eq. 4.14)}$$

$$k_{eff} = \frac{Ql_1}{l_2 w|T_2 - T_1|} \quad \text{(Eq. 4.15)}$$

To find the thermal conductivity of the composite model with gyroid, the total heat flux Q in Watts is attempted to be acquired from the heat transfer analysis in Abaqus. The total heat flux can be obtained by the sum of the HFL or heat flux at nodes. However, this calculation was difficult to be conducted without an error in Abaqus due to a large number of nodes in the mesh. Thus, the heat flow analysis from Abaqus needs to be repeated and improved in the future work.

### 4.5.6. Visualization of the Results

From the Abaqus analysis, the following outputs can be obtained: HFL (heat flux vector at integration points), NT (nodal temperature at each node), and RFL (reaction fluxes at nodes). Fig 4.9 shows the HFL result for the unit model and Fig. 4.10 shows the NT result: the 2D (A), the 3D (B), and the sectional cut of the 3D model to visualize the inside the model (C). Fig 4.11 shows the RFL results: the 3D view (A), and the sectional cut (B).

As shown in Fig. 4.9 for the HFL result, the heat flux largely occurs in the gyroid, which is expected since the gyroid in the model has the higher thermal conductivity as compared to the air. The temperature gradient as shown in Fig. 4.10 is expected as the all the components are designed as solid, and thus the temperature vary between the two aluminum plates. If the air were modeled as fluid instead, the nodal temperature distribution would have been more uniformed in the air with continuity. Nonetheless, the model used in this study resulted with the following visualization, although the numerical data for the results were not able to be exported due to the large mesh size and computational limitations.

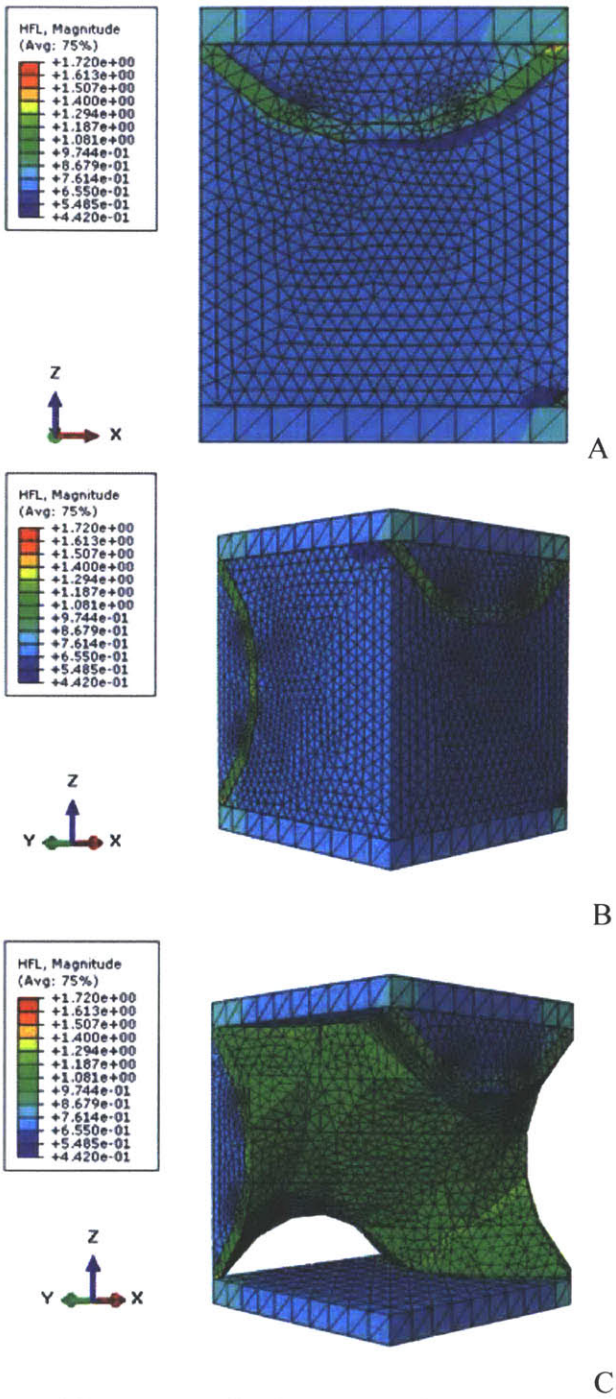


***Figure 4.9**: Visualizations of the HFL result: the 2D (A), the 3D (B), and the sectional cut of the 3D model (C).*

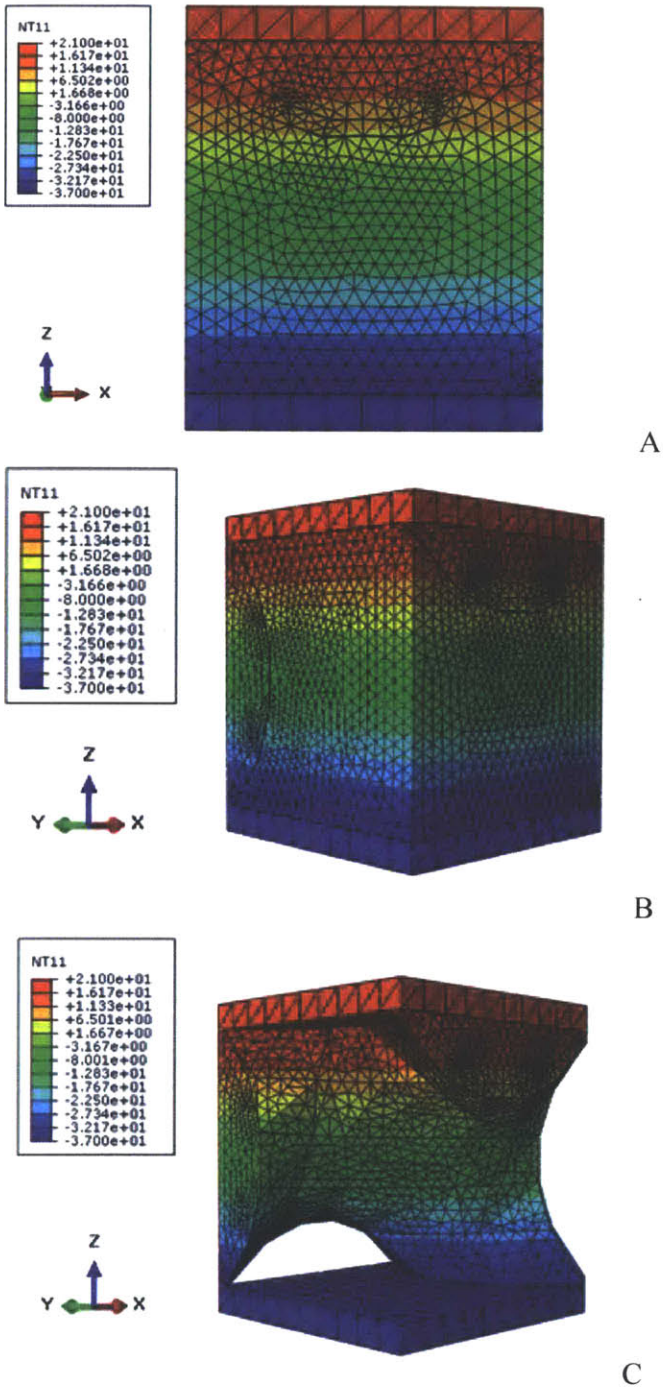


***Figure 4.10**: Visualizations of the NT result: the 2D (A), the 3D (B), and the sectional cut of the 3D model (C).*

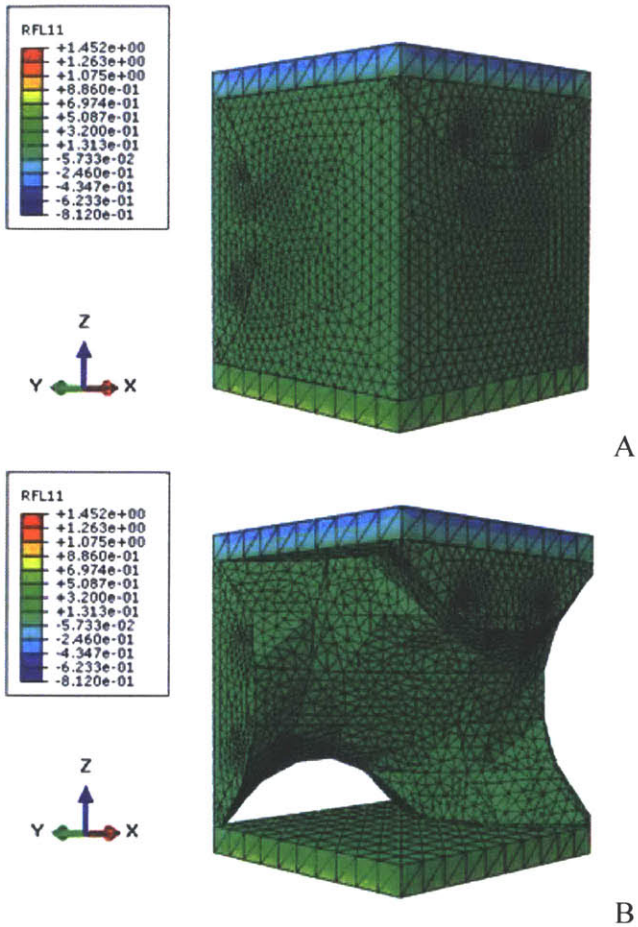


***Figure 4.11**: Visualizations of the RFL results: the 3D (A), and the sectional cut of the 3D model (B)*

### 4.5.7. Future Work

The heat flow analysis in Abaqus requires several refinements as to be completed. First, the mesh quality of the entire model can be refined while remaining in the workable range as to even to perform convergence test by increasing the number of meshes. Manipulating the mesh quality may enable the computation of the total heat flux without errors. Secondly, the calculated conductivity should be compared with the air-only conductivity and the filling-material-only conductivity: the value should be in between the two values. Also, the calculated conductivity should be compared to a theoretical value obtained from the thermal conductivity equation for open cell structure (Eq. 4.11).

With an assumption that radiation and convection effects are negligible, the model has only solid volumes even for the air in the cavity; however, the continuity of cavity in the gyroid model could allow the airflow within the mullion section. For the airflow to be accounted, the convection effect may be considerable. Moreover, as the gyroids in a smaller scale with low relative density, the radiative heat transfer can be significant (Coquard et al. 2008).

## 4.6. Heat Flow Test

In order to obtain physical experimental values for thermal conductivity of a gyroid structure with air in the cavity, the heat flow test is carried out with the Heat Flow Meter (HFM) 436 Lambda by Netzsch. The HFM with its cold plate and hot plates inside of the insulated container calculates thermal conductivity, thermal resistance, and temperature gradient for a given temperature range. The size of the test specimen is 30cm by 30 cm by 10cm at its maximum, and 10cm by 10cm by x cm at its minimum (the minimum height of the specimen is not necessarily defined). Thus, before testing the 3D models printed by ZCorp, a 10cm-by-10cm-aluminum block surrounded styrofoam blocks is tested first to check the reliability and workability of the machine. During this study, the results from the heat flow test were not satisfactory, as the thermal conductivity of the aluminum block does not match the known property of aluminum. The output result for the thermal conductivity was implying that the thermal conductivity of the styrofoam blocks around the aluminum specimen was accounted for. Ideally, the result was expected to account the specimen only and with the value for the aluminum alloy. As the test could not be completed successfully, the heat flow test requires future works to be completed.


***Figure 4.12**: Heat Flow Meter (HFM) 436 Lambda by Netzsch (Left) and initial test specimen of 10cm by 10cm by 2.5 cm aluminum block surrounded by styrofoam blocks for the entire specimen sized as 30 cm by 30 cm by 2.5 cm.*

## 4.7. Concluding Remarks on Experiments and Simulations

The mechanical experiment with 3D printed gyroid structures resulted with a scaling relation that is comparable with other experimental data. However, as with the difficulty in using the equipment properly and managing the heavy computation in computational analysis, the theoretical thermal conductivity of a gyroid could not be compared with experimental data. Nonetheless, the following two equations of gyroid properties are obtained and prepared for the later chapter, where evaluation of different densities of gyroid is conducted.

$$\frac{E}{E_s} = \left(\frac{\rho}{\rho_s}\right)^{2.73\pm0.09} \quad \text{(Eq. 4.5)}$$

$$k_{eff,c} = \phi k_f + \frac{1}{3}(1-\phi)k_s \quad \text{(Eq. 4.11)}$$

# Chapter 5. Design and Optimization of Mullion System

In this chapter, the topology optimization for both structural performance and thermal performance is conducted with the calculated structural and thermal properties for selected relative densities.

## 5.1. Performance Optimization Overview

As studied in Chapter 3, a higher relative density gyroid structure increases the Young's modulus, thus the stiffness as well; however, it also increases its thermal conductivity. Thus, some structural strength requires being compensated for better thermal resistance. The relationship between the two objectives, the structural performance and the thermal performance, is studied with the objective space, and the best-fit solutions are suggested at the end of the chapter.

## 5.2. Problem Statement

### 5.2.1. Variables

The variables used in the performance optimization are the relative densities of gyroid for their designated slices within a curtain wall mullion. Table 5.1 lists the relative densities selected for the optimization study: $i$ is the identifier and $\varepsilon$ is the relative densities, calculated from the Rhino/GH models shown in Figure 5.1. For the variance of the densities, two different modules are investigated: one with five variable relative densities, and the other with seven variable relative densities. For this multi-objective design problem, $J_1$ is named for the structural performance measure and $J_2$ for the thermal performance measure; Likewise, $w_1$ is the weight of the $J_1$ in the composite objective function, and $w_2$ is that of the $J_2$. Table 5.1 lists the ten different composite objective functions with varying weights used in the study, and the results are plotted in the objective space.

| $i$ | $\varepsilon$ |
|---|---|
| **0** | 0.095 |
| **1** | 0.127 |
| **2** | 0.156 |
| **3** | 0.187 |
| **4** | 0.242 |
| **5** | 0.345 |

***Table 5.1*** *Relative densities of gyroid structure used in the optimization study.*

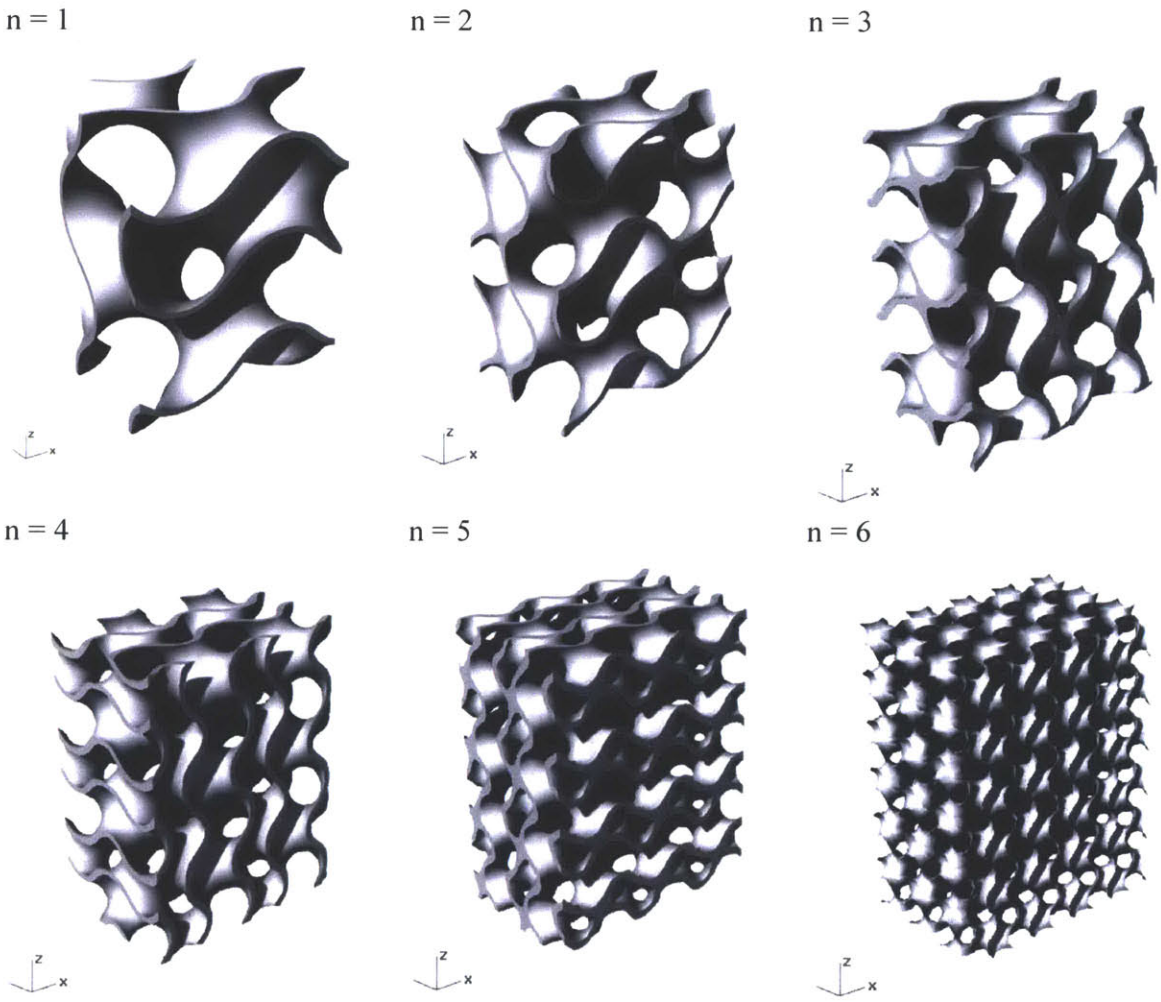


***Figure 5.1****: Rendered images of various densities of gyroid structures with 0.125" thickness in 1" by 2.25" by 3" block (a gyroid surface for n =6)*

## 5.2.2. Constraints

As to constraint the geometry of the section for the efficient topology optimization, a conventional curtain wall mullion cross-section is simplified and used for the outer boundary of the gyroid. The model remained to have 1/8"-thick plastic (or less conductive material) plates that cover the entire cross-section to have an enclosed section of the mullion: the boundary plates would eliminate the water-penetration problems and encase the section firmly intact. The section within the boundary plates is divided into slices in the horizontal direction: 9 slices for the Module 1 and 13 slices for the Module 2 (Fig. 5.2). Other topologies of slices subjected for optimization are initially considered additionally: alt.1) a vertically sliced section, and alt.2) a section sliced by the offset boundary lines as shown in Figure 5.3. However, the vertically sliced section does not yield many variations of densities as in the optimized solution as the slices are placed in parallel. The other module with the offset boundary lines is saved for the future work, as the module requires 2D thermal resistance calculation or more slicing to use 1D resistance calculation.

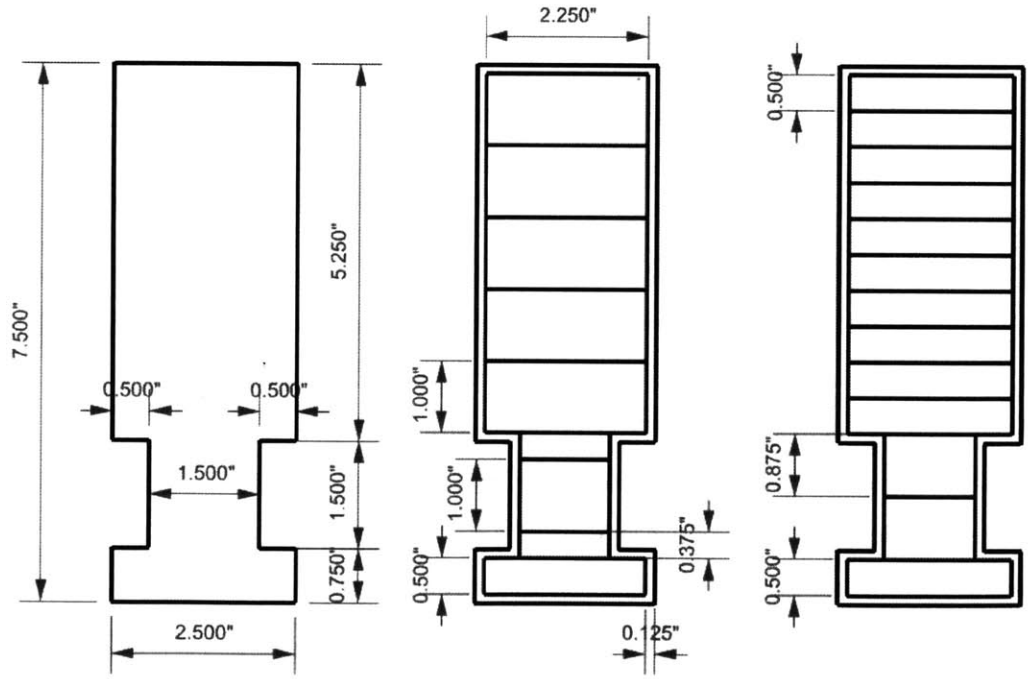


***Figure 5.2**: Geometry of the boundaries used for the optimization study: the outer boundary (Left), Module 1 (Middle), and Module 2 (Right).*

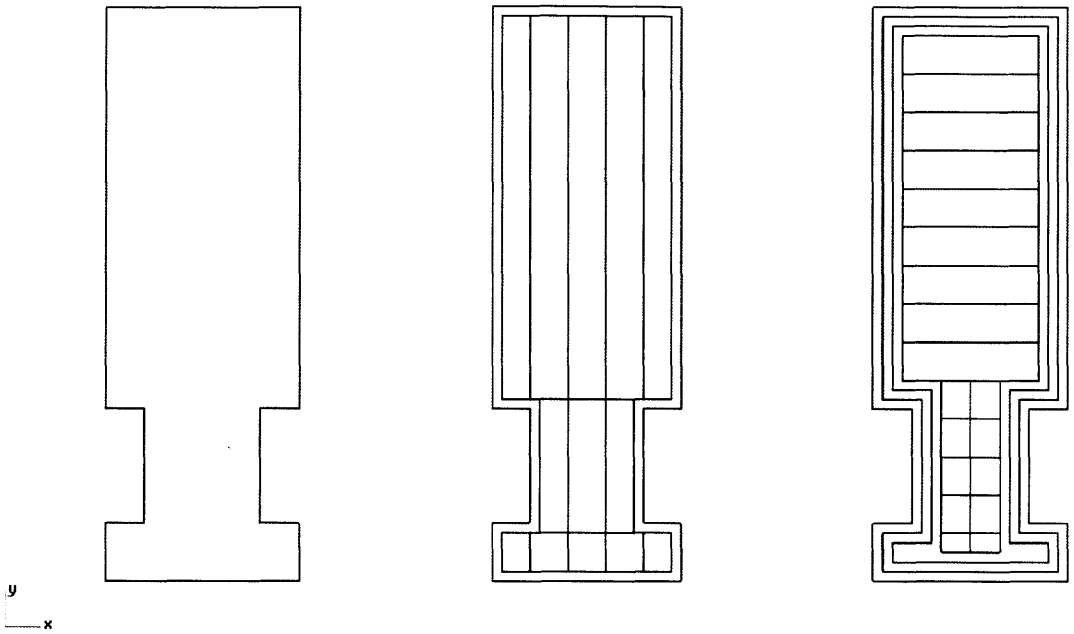


***Figure 5.3**: Alternative geometries considered initially for the optimization study: the boundary (Left), the vertically sliced module alt. 1 (Middle), and the module with the offset boundary lines (Right).*

### 5.2.3. Objectives

The following two objectives are considered in this design optimization problem:

1. To maximize the structural performance
2. To maximize the thermal performance

The structural performance, or the structural stiffness of each module, is measured by the product of the Young's modulus and the second moment of inertia: the young's modulus is calculated with Eq. 4.5 from Chapter 4, and the second moment of inertia is calculated using the Transformed Area Method (as described in 5.2.5.1). Meanwhile, the thermal performance is measured by the sum of the thermal resistance using the thermal resistance network concept for heat transfer or the electrical analogy (as described in 5.2.5.3). The structure performance measure is called $J_1$, and the thermal performance measure is called $J_2$.

### 5.2.5. Composite Objective Functions

To study the relationship between the two objectives, several different composite objective functions (COFs) with various weights for both objectives are utilized. The composite performance measure used for the optimization can be expressed as follows:

$$\max F, \quad where\ F = J_1 w_1 + J_2 w_2 \qquad \text{(Eq. 5.1)}$$

The weight for the first objective, $w_1$, and the weight for the second objective, $w_2$, are selected accordingly as the un-weighted, pure values are in a different magnitude. Table 5.2 lists the various COFs used in the optimization:

| Comp. Obj. Function | $w_1$ | $w_2$ |
|---|---|---|
| **1** | 1 | 0 |
| **2** | 1 | 1 |
| **3** | 1 | 10 |
| **4** | 1 | 50 |
| **5** | 1 | 60 |
| **6** | 1 | 70 |
| **7** | 1 | 150 |
| **8** | 1 | 175 |
| **9** | 1 | 200 |
| **10** | 1 | 250 |
| **11** | 1 | 300 |
| **12** | 1 | 400 |
| **13** | 1 | 450 |
| **14** | 1 | 500 |
| **15** | 1 | 600 |
| **16** | 0 | 1 |

***Table 5.2**: List of Composite Objective Functions (COFs) and the weights for both objectives.*

### 5.2.6. Assumptions and Calculation Methods

#### 5.2.6.1. Transformed Section Method

When calculating the structural measure for each design, the transformed section method is used as the slices within a composite design have various values for the Young's modulus. The slices, including the intermediate regions, are assumed to homogenous for the stiffness calculation using the transformed section method: when calculating Young's modulus, the intermediate

regions are calculated with the average relative density of the neighboring regions. The transformed section method is used in the GH code as described in this section.

Primarily, the basic calculations of area and for each slice in the section are carried out by the default grasshopper components. For instance, in the designed Grasshopper codes, the following values are computed using a component called "Area Moments (AMoments):" the area of i-th slice, $A_i$, the distance from the x-axis to the local centroid of the area, $y_i$, and the area moment of inertia relative to its centroid, $I_i$.

For an i-th designed gyroid slice, the ratio of the Young's modulus for the i-th slice to the minimum value of the Young's moduli of the slices is calculated.

$$n_i = \frac{E_i}{E_{min}} \quad \text{(Eq. 5.2)}$$

The transformed areas of the slices are then calculated by multiplying $n_i$ to the area for an i-th slice.

$$A_{t,i} = n_i A_i \quad \text{(Eq. 5.3)}$$

Using the transformed areas, the distance between the neutral axis of the transformed composite section and the x-axis, $y_c$ is calculated as the following:

$$y_c = \frac{\sum y_i A_{t,i}}{\sum A_{t,i}} \quad \text{(Eq. 5.4)}$$

The area moment of inertia for the i-th slice is also transformed by multiplying $n_i$.

$$I_{t,i} = n_i I_i \quad \text{(Eq. 5.5)}$$

Relative to the global neutral axis of the composite section, the area moment of inertia for the i-th slice is then calculated:

$$I_{t,n.a.,i} = A_{t,i} {d_i}^2 + I_{t,i} \quad \text{(Eq. 5.6)}$$

The total area moment of inertia of the composite section is calculated by summing the transformed area moment of inertia of each slice with respect to the neutral axis as the following:

$$I_{global} = \sum I_{t,n.a.,i} = \sum \left(A_{t,i} {d_i}^2 + I_{t,i}\right) \quad \text{(Eq. 5.7)}$$

where $d_i$ is the distance between the centroid of i-th slice and the neutral axis of the transformed composite section.

$$d_i = |y_c - y_i| \quad \text{(Eq. 5.8)}$$

Lastly, the stiffness measure of the composite section is calculated as the following:

$$Stiffness\ Measure = \sum E_{min} I_{t,n.a.,i} = J_1 \quad \text{(Eq. 5.9)}$$

This stiffness measure is then used as the first objective value, $J_1$, which is subjected to be maximized for the optimization.

### 5.2.6.2. Suppressed Convection Effects

To suppress the effects of the heat transfer due to convection in the composite section, the sections are mostly divided into slices with 0.5 in thickness, which is the distance between two plates where convection effects are at its minimum (see the graph in Fig 5.4). For the Module 1, 1 in-thick slices are used for simplified model: 1 in thickness also has relatively low convection effect as shown in the following graph.

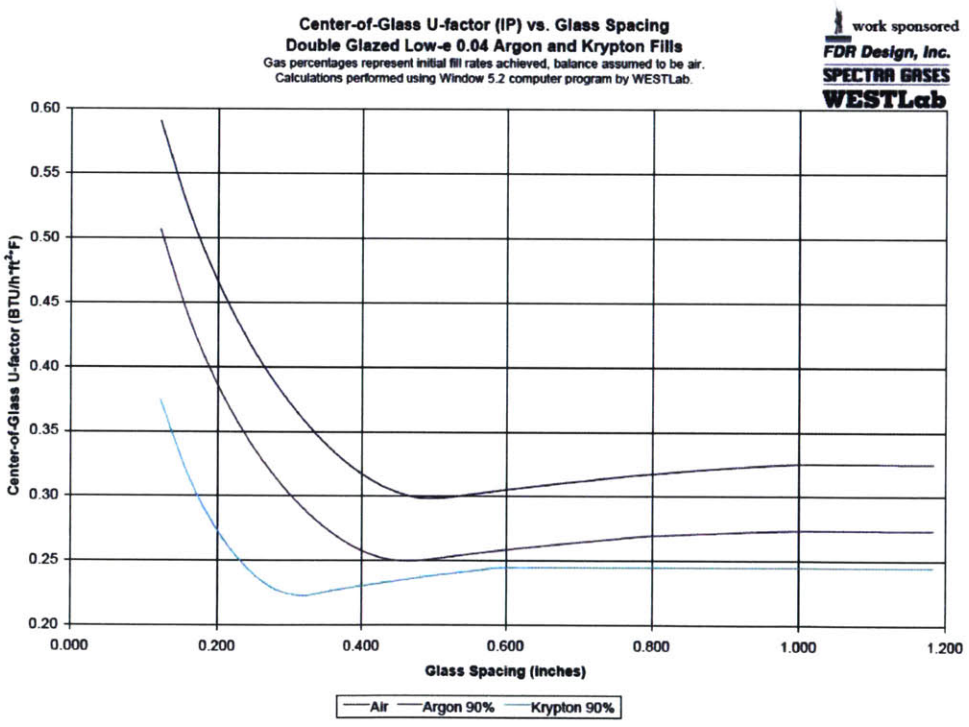


***Figure 5.4**: Center-of-Glass U-factor vs. glass spacing with air, argon and krypton fills (Courtesy of Wilson 2012).*

### 5.2.6.3. Thermal Resistance Network Concept

Using the thermal resistance network concept for heat transfer or the electrical analogy with Ohm's law, the thermal resistances of the designed sections are calculated. In general, for heat transfer calculation through a wall, the following equations are used (Çengel et al. 2015). Figure 5.5 illustrates the thermal resistance network concept with the electrical analogy that are used for heat transfer in wall.

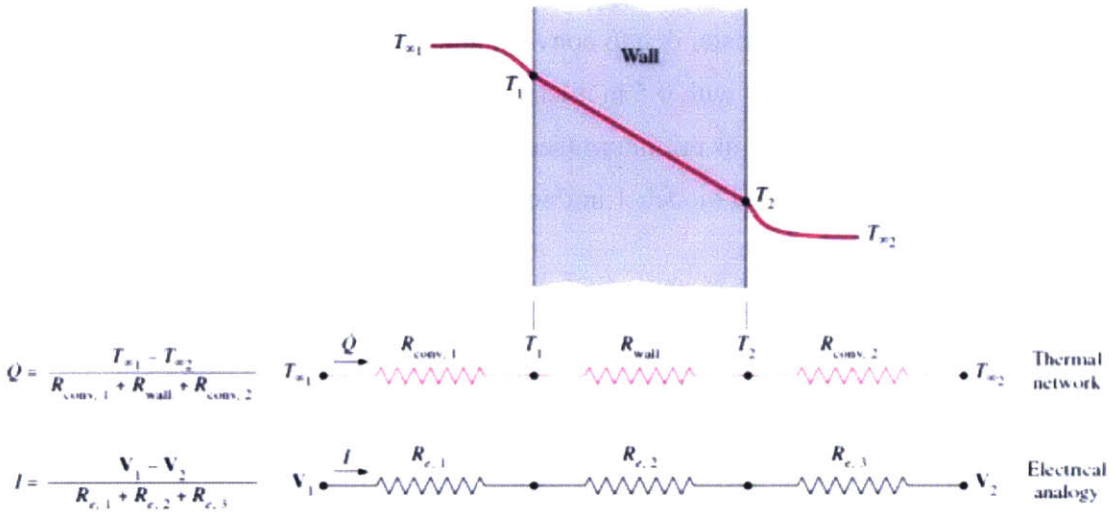


***Figure 5.5**: The thermal resistance network concept used in a wall (Courtesy of Çengel et al. 2015).*

Similarly, the rate of the heat transferred through a designed section can be calculated as follow (Çengel et al. 2015):

$$\dot{Q} = \frac{T_1 - T_2}{R_{total}} \qquad \text{(Eq. 5.10)}$$

, where $T_1$ is the interior temperature, $T_2$ is the exterior temperature, and $R_{total}$ is the thermal resistance of the entire section that lies in the direction of the heat transfer. The $R_{total}$ can be calculated as the following (Çengel et al. 2015):

$$R_{total} = R_{conv,1} + R_{designed\ section} + R_{conv,2} = \frac{1}{h_1 A} + \frac{L}{kA} + \frac{1}{h_2 A} \qquad \text{(Eq. 5.11)}$$

, where the convective heat transfer coefficient for the interior air is $h_1$; for exterior, $h_2$; the thermal conductivity of the designed section is $k$; the area is $A$; and the thickness along the heat transfer direction is $L$. In this study, as the convection effects are considered as negligible,

$R_{conv,1}$ and $R_{conv,2}$ are disregarded and only the convection is accounted as the following (Çengel et al. 2015):

$$R = \frac{L}{kA} \quad \text{(Eq. 5.12)}$$

According to the thermal resistance network concept for heat transfer, for n-series of resistance in one direction, the thermal resistance of the composite section can be calculated as (Çengel et al. 2015):

$$R_{total} = R_1 + R_2 + R_3 + R_4 + \cdots R_n \quad \text{(Eq. 5.13)}$$

Therefore, in the Module 1,

$$R_{composite\ section} = R_1 + R_{1.5} + R_2 + R_{2.5} + R_3 + R_{3.5} + R_4 + R_{4.5} + R_5 \quad \text{(Eq. 5.14)}$$

When Eq. 5.14 is substituted for each R value,

$$R_{composite\ section} = \frac{L_1}{k_1 A_1} + \frac{L_{1.5}}{k_{1.5} A_{1.5}} + \frac{L_2}{k_2 A_2} + \frac{L_{2.5}}{k_{2.5} A_{2.5}} + \frac{L_3}{k_3 A_3} + \frac{L_{3.5}}{k_{3.5} A_{3.5}} + \frac{L_4}{k_4 A_4} + \frac{L_{4.5}}{k_{4.5} A_{4.5}} + \frac{L_5}{k_5 A_5} \quad \text{(Eq. 5.15)}$$

As from the given geometry for the Module 1,

$$L_1 = L_{1.5} = L_2 = L_{2.5} = L_3 = L_4 = 1" = L$$

$$L_{3.5} = L_{4.5} = 0.375" = 0.375L$$

$$L_5 = 0.5" = 0.5L$$

$$A_1 = A_{1.5} = A_2 = A_{2.5} = A_3 = A_5 = A$$

$$\text{, and } A_{3.5} = A_4 = A_{4.5} = \left(\frac{1.25"}{2.25"}\right) A = 0.556\,A$$

So Eq. 5.15 can be rewritten as the following:

$$R_{composite\ section} = \left(\frac{L}{A}\right)\left(\frac{1}{k_1} + \frac{1}{k_{1.5}} + \frac{1}{k_2} + \frac{1}{k_{2.5}} + \frac{1}{k_3} + \frac{0.375}{0.556k_{3.5}} + \frac{1}{0.556k_4} + 0.3750.556k4.5+0.5k5\right) \quad \text{(Eq. 5.16)}$$

$$\frac{R_{composite\ section}}{\left(\frac{L}{A}\right)} = \left(\frac{1}{k_1} + \frac{1}{k_{1.5}} + \frac{1}{k_2} + \frac{1}{k_{2.5}} + \frac{1}{k_3} + \frac{0.375}{0.556k_{3.5}} + \frac{1}{0.556k_4} + 0.3750.556k4.5+0.5k5\right) \quad \text{(Eq. 5.17)}$$

As for the measure of thermal performance, the right side of Eq. 5.17 is used.

$$J_{2,M1} = \left(\frac{1}{k_1} + \frac{1}{k_{1.5}} + \frac{1}{k_2} + \frac{1}{k_{2.5}} + \frac{1}{k_3} + \frac{0.375}{0.556k_{3.5}} + \frac{1}{0.556k_4} + \frac{0.375}{0.556k_{4.5}} + \frac{0.5}{k_5}\right) \quad \text{(Eq. 5.18)}$$

The objective $J_2$ is subjected to be maximized for a higher thermal resistance of the designed composite section. Similarly, for the Module 2 with total of 13 slices,

$$R_{composite\ section} = \frac{L_1}{k_1A_1} + \frac{L_{1.5}}{k_{1.5}A_{1.5}} + \frac{L_2}{k_2A_2} + \cdots + \frac{L_5}{k_5A_5} + \frac{L_{5.5}}{k_{5.5}A_{5.5}} + \frac{L_6}{k_6A_6} + \frac{L_{6.5}}{k_{6.5}A_{6.5}} + \frac{L_7}{k_7A_7} \quad \text{(Eq. 5.19)}$$

Based on the geometry of the Module 2,

$$L_1 = L_{1.5} = L_2 = L_{2.5} = \cdots = L_5 = L_{5.5} = L_7 = 0.5" = L$$

$$L_6 = L_{6.5} = 0.875" = 0.875L$$

$$A_1 = A_{1.5} = A_2 = A_{2.5} = \cdots = A_5 = A_{5.5} = A_7 = A$$

$$\text{, and } A_6 = A_{6.5} = \left(\frac{1.25"}{2.25"}\right)A = 0.556\,A$$

When the values above are substituted and the equation above is rearranged,

$$\frac{R_{composite\ section}}{\left(\frac{L}{A}\right)} = \left(\frac{1}{k_1} + \frac{1}{k_{1.5}} + \frac{1}{k_2} + \frac{1}{k_{2.5}} + \cdots + \frac{1}{k_5} + \frac{1}{k_{5.5}} + \frac{0.875}{0.556k_6} + \frac{0.875}{0.556k_{6.5}} + \frac{1}{k_7}\right) \quad \text{(Eq. 5.20)}$$

$$J_{2,M2} = \left(\frac{1}{k_1} + \frac{1}{k_{1.5}} + \frac{1}{k_2} + \frac{1}{k_{2.5}} + \cdots + \frac{1}{k_5} + \frac{1}{k_{5.5}} + \frac{0.875}{0.556k_6} + \frac{0.875}{0.556k_{6.5}} + \frac{1}{k_7}\right) \quad \text{(Eq. 5.21)}$$

## 5.3. Methodology

(1) A conventional mullion section design is selected and divided into slices for optimization. In Module 1, the section is divided into nine slices (5 with variable relative densities and the rest four slices as the intermediate slices). In Module 2, the section is divided into 13 slices (7 with variable relative densities and the rest six slices as intermediate slices). As shown in Figure 5.6, the slices with variable relative densities are named as 1, 2, 3, 4, and 5, while the intermediate slices are named as 1.5, 2.5, 3.5, and 4.5. Similarly, Module 2 is modeled as shown in Figure 5.6.

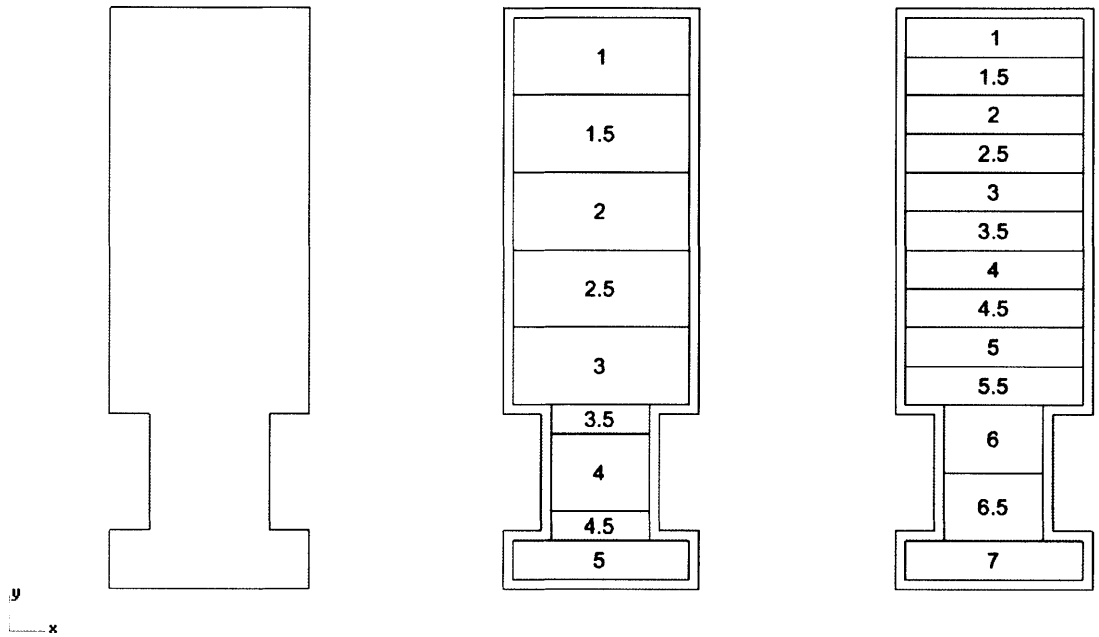


*Figure 5.6: Labeled slices for Module 1 (Middle) and Module 2 (Right) with the boundary geometry (Left)*

(2) The slices are then assigned with different relative densities of gyroid. The intermediate slices are designated with the average value of the relative densities of the neighboring two slices.

(3) Stiffness is measured as the product of the Young's modulus (from experiment values) and second moment of area (from a composition of each design) for each section. The stiffness of the entire 2D section of the mullion is then calculated for structural performance evaluation.

(4) Thermal resistance values calculated for each slice, and the total thermal resistance value is calculated using Eq. 5.18 for Module 1 and Eq. 5.21 for Module 2 as the thermal performance measure. The heat flow for each design is simplified as a 1D Heat flow for calculation.

(5) With the following composite objective functions as show in Table 5.2, the performance measures are evaluated, and using a GH optimization component "Goat," the performance measure is subjected to be maximized.

(6) For readability, each topology solution is expressed in color-coded, redder being denser slice.

(7) As with different composite objective functions, the optimized topologies of gyroids are evaluated, and the solutions are plotted in objective space for comparison.

## 5.4. Modeling Intermediate Regions

As am performance-optimized composition of the relative densities of gyroids is designed, the intermediate sections within the composite section require additional refinements in modeling. An intermediate slice is a slice in between two gyroid slices with different relative densities. As the relative density varies in one direction within the intermediate slice, several methods are attempted including 1) modifying the mathematical equation of a gyroid surface, and 2) manipulating generated gyroid surfaces. The modified equation is first used in Matlab with randomly distributed points; however, the output was not as desired for its difficulty in visualizing and understanding the result. To quickly visualize the generated surface of the modified equation, the Grasshopper script with "IsoSurface" used in Chapter 3 is modified with the new equation. As the results by modifying the equation were not so desirable, the generated gyroid surfaces are transformed and modified using a built-in Grasshopper component to create intermediate surfaces. The second method by transforming the generated surfaces is preferred in this study for the further steps for its rapid modeling.

### 5.4.1. Modifying the Mathematical Equation of Gyroid

A single-gyroid surface can be expressed as:

$$\sin(x)\cos(y) + \sin(y)\cos(z) + \sin(z)\cos(x) = 0 \qquad \text{(Eq. 2.9)}$$

As the density of the gyroid is desired to be varied in one direction, the gyorid equation is modified to be the following equation:

$$\sin(x)\cos(Ay) + \sin(Ay)\cos(z) + \sin(z)\cos(x) = 0 \qquad \text{(Eq. 5.22)}$$

where A is a function of $y$:

$$A = f(y) = ay + b \qquad \text{(Eq. 5.23)}$$

For instance, a = 0.1 and b = 1 are used in Eq. 5.23:

$$\sin(x)\cos(0.1y^2 + y) + \sin(0.1y^2 + y)\cos(z) + \sin(z)\cos(x) = 0 \qquad \text{(Eq. 5.24)}$$

The surface using Eq. 5.24 is then plotted in Rhino/Grasshopper as shown in Fig. 5.7.

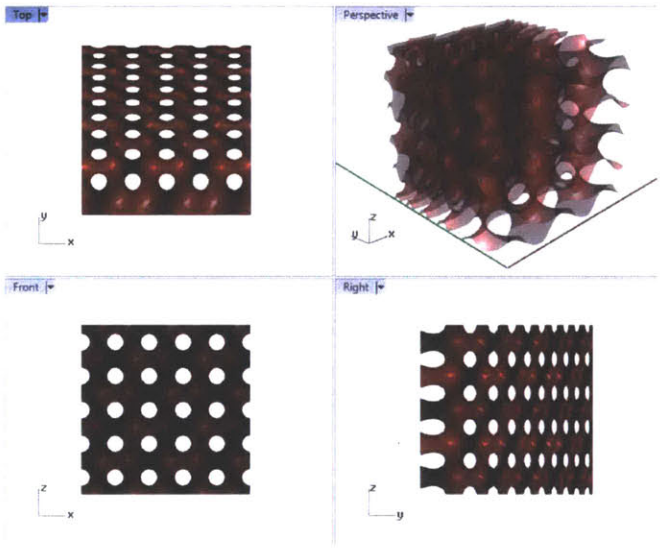


***Figure 5.7**: Modified gyroid surface using Eq. 5.24.*

Even though the mathematical equation sounds reasonable, the resulted surface was not satisfactory for the usage in the model; undesirable results could be due to the graphing method in Rhino/GH, and yet the mathematical equation may need further revision and improvements.

### 5.4.2. Using a "Morph" Component in Rhino/Grasshopper

To reduce the complexity in math and the modeling time, a Grasshopper script is written to utilize a built-in Grasshopper component called "Morph," which transforms an input geometry with respect to the reference geometry and the target geometry. In the written script for this study, the reference geometry is a cube that is used in the earlier Grasshopper script described in Chapter 3. The target geometry or the target volume is a box-like volume with a base surface of a trapezoid as shown in the following figure (Fig 5.8).

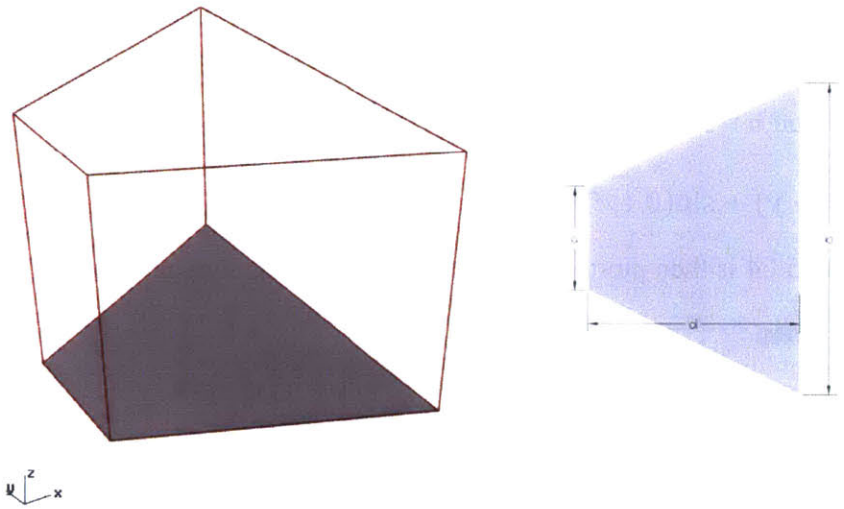

***Figure 5.8**: Target volume used for morphing: 3D view (Left) and the base geometry with dimensions (Right)*

The neighboring two gyroid surfaces that are subject to be connected with the intermediate surface affects the dimensions of the base trapezoid: the ratio of the length of the shorter side "an" and the longer side "b" of the base trapezoid is the ratio of the numbers of periods for two neighboring gyroid surfaces (Figure 5.8). Note that it is not the ratio of the relative densities of the gyroid surfaces. Also, the distance between the parallel sides of the base trapezoid, "d" in the Figure 5.8, should be equal to the depth of the intermediate gyroid slice. And the length of the shorter side of the two parallel sides in the base trapezoid, "a" in the Figure 5.8, should be equal to the width of the intermediate gyroid slice.

When constructing the target volume, one needs to be careful of choosing the proper method and components. In Grasshopper, a box or a volume can be constructed in several different ways: one

popular way to construct a box-like volume is by extruding a base surface. The base surface can be constructed by using "4Point Surface," for a trapezoid or any other similar built-in surface generating components in Grasshopper. This method of creating a volume by extruding a surface is rather a simpler way to construct a volume. However, in this case of a box volume with a trapezoid base, the "extruding a surface" method creates an error due to how the Grasshopper recognizes the output, extruded volume. The eight corner points for the extruded surface, or even for the twisted box volume defined by "Surface Box (SBox)," does not match the eight corner points for the target volume: the generated corner points, instead, are located at the corners of the very outer rectangle box that can enclose the desired target volume (Fig. 5.9).

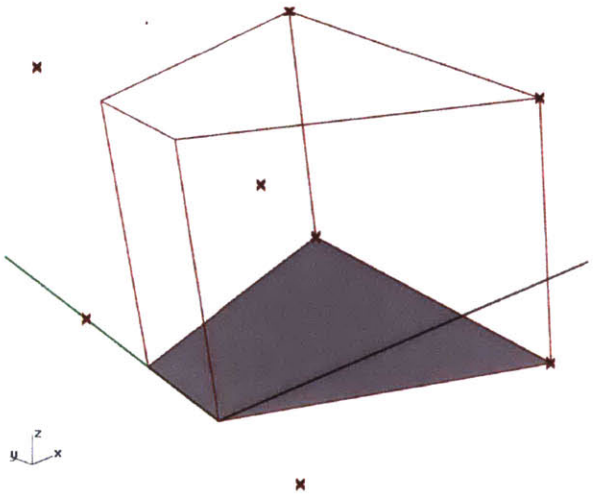

***Figure 5.9**: Error: the corner points recognized from the volume defined by "SBox."*

Thus, when the volume created by extruding the base surface is connected to the "Morph" component; the output, morphed geometry does not fit in the desired target volume. In order to avoid such a problem, the target volume for morphing is constructed by using a "Twisted Box (B)" component. In other words, the eight corners define the target box volume. After the target box is carefully constructed, the original reference box that encloses gyroid and the gyroid along with the target box are used as input data for a Morph component. The Morph component then outputs a transformed gyroid (Fig. 5.10 and Fig 5.11) that can be trimmed to be an intermediate section.

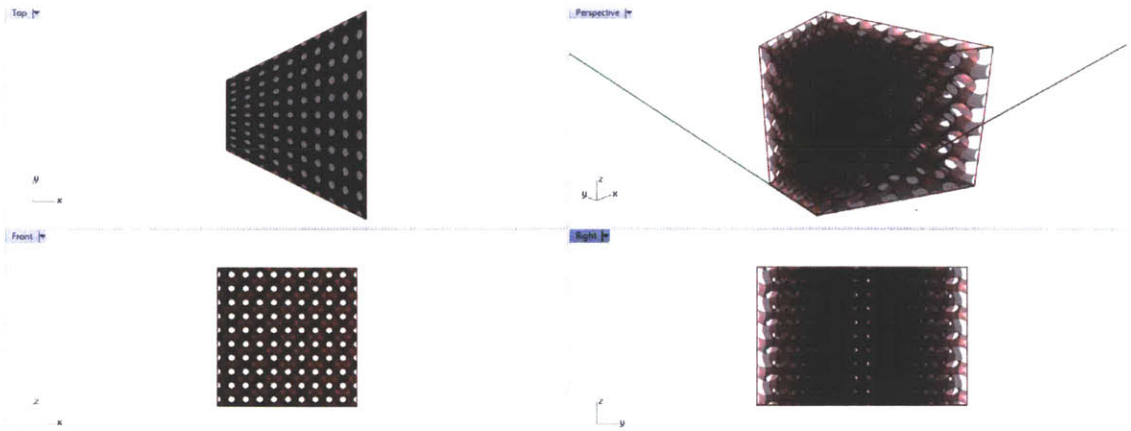

***Figure 5.10**: Morphed gyroid surface in the twisted box.*

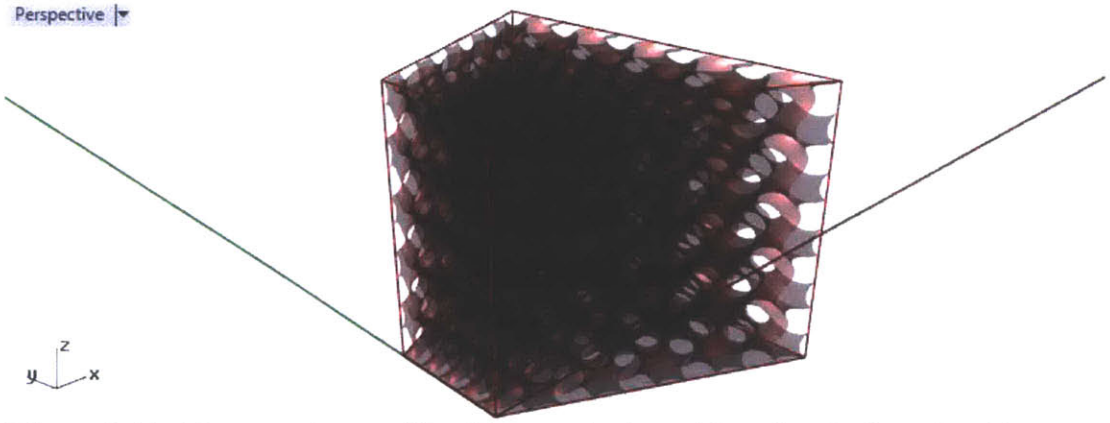


***Figure 5.11**: Close up view on 3D of the morphed gyroid surface in the twisted box.*

Morphing method using Grasshopper components can quickly model the varying density of gyroid in a targeted volume once the script is carefully written as stated above. However, the script can be refined further so that the generated gyroid surface of the intermediate region can smoothly meet the adjacent gyorid surfaces. As from the written script in this study, the surface connection needs to be manually checked and refined by cutting the "right" slices from the gyroid cube generated by the Grasshopper script described in Chapter 3. In other words, the lines on the cut face of the intermediate gyroid surface and the lines of the cut face of the adjacent gyroid surfaces have to coincide or at least overlap to a reasonable degree when extruded with a thickness. For the future development, the morphing method can be improved by conducting the four core processes in one script: 1) generating gyroid surface, 2) creating intermediate gyroid surfaces, 3) cutting the generated gyroid surfaces in the proper location, and 4) placing the

gyroid surfaces as the optimized solution from the optimization process. The resulted composite gyroid surface then can be extruded to have a thickness and be ready for 3D printing.

### 5.4.3. Results and Discussion

The optimized solutions for the COFs in Table 5.2 resulted as shown in Table 5.3 for Module 1 and Table 5.4 for Module 2. In the tables, some values are omitted as the solutions were repeated with the solution for the previous COF. The optimized solutions were graphically represented in Fig. 5.12 and 5.13.

The overall trend of the topology solutions is that as the objective weighs the thermal performance measure more, the lighter densities are selected, starting from the mid-section: the optimized solutions for the COF #3 to #6 in Module 1 illustrate clearly the trend of having lighter sections from the mid-section. Similarly, the results for Module 2 show that the higher thermal performance objective weight, the lighter overall section is.

In the meanwhile, the solutions do not merely suggest placing lighter slices in the middle of the section; in fact, based on the optimization runs, multiple options for the topology to increase the thermal performance may exist. While running the optimization using the GH component, Goat, the results varied as how the optimization process was carried out. When the local, quadratic approximations (BOBYQA) algorithm is performed alone with an input, parameter set of random numbers, the suggest solution might have a relatively high performance measure but does not necessarily the maximum performance measure. Thus, to find the design with maximum performance value within a reasonable time, the global, evolutionary (CRS2) algorithm is used primarily as to account the overall tendency of the solutions and their objectives. Then, the local, quadratic approximation algorithm is utilized to find the local maxima around the temporary solution suggested by the evolutionary algorithm. By using the two algorithms consecutively, instead of one, the suggest solution is well approximated to the design with the true maximum performance value.

The multiple local maximum for the performance in design may influence the results in that some results have more distributed relative densities than others. For instance, when the solution for the COF#15 is compared to that for the COF#14 in Module 1, the slice 5 has lighter gyroid while the slice 1 has denser gyroid. In other words, although the overall trend of using lighter slice to improve the thermal performance still exists, the solution for the COF#15 suggests

having more distributed relative densities instead of using a lighter gyroid for the slice 1 only or 5 only. Similar trend of having more well-distributed densities can be found in the solution of the COF#7 and 12 in Module 2, when each solution is compared with the previous one, the solution for the COF#6 and #11. Even though these well-distributed solutions may not have the true maximum performance value, the well-distributed solutions are more preferable for manufacturing and production of the solutions, as the change in relative densities of the gyroid is smoother.

In addition, the existence of multiple local optima in performance may have influenced some resulted optimized solution to be the local maxima not the global maxima. For example, when the COF #4 in Module 2 is compared with the COF #5 in Module 2, even though $J_1$ is weighted heavier than $J_2$, the solution for the COF#4 has lower $J_1$ value with higher $J_2$; instead, $J_2$ for the COF #4 in Module 2 is higher than the COF #5 in Module 2. In other words, the objective values for both $J_1$ and $J_2$ of the COF #4 in Module 2 does not match with the expectation of having higher $J_1$ value as compared to the COF #5 in Module 2. This error may be due to the time used for optimization process. If the time for optimization process in Goat is increased to more than a minute, the result of the optimized solution for the COF #4 in Module 2 would have a higher $J_1$ value, following the trend found from the rest of the results.

To study the relationship between the two objectives, the structural performance measure and the thermal performance measure, the objective space is plotted in Fig. 5.14. As shown in the graph, as the thermal performance decreases, the structural performance tends to increase. The degree of change in the thermal performance is smaller than in the structural performance: in other words, the small change in the thermal performance largely affects the structural performance of the design.

Also, the thermal performance measures from Module 2 are higher than Module 1, whereas the ranges of the structural performance for both Modules mostly overlap with each other. This difference in the values for the thermal measures is due to how $J_2$ is defined: $J_2$ is not the absolute thermal resistance value but instead is the thermal resistance divided by the ratio of the length of each slice over the area of the slice perpendicular to the heat transfer direction. Thus, it is noted that the values of $J_2$'s of the two Modules are not comparable.

In the results where the structural performance measure is weighted relatively heavier than the thermal performance measure, the locations, where glass panels are connected (slice 4 of Module

1 and slice 6 of Module 2,) have composite gyroids with relatively high densities. Those high-density slices can act as a thermal bridge if the shell for the region connected to the glass panels is not carefully designed. The vacuum of the glass does not align with the least dense foam; it may still be possible for heat to escape across the mullion support and through the outer glass panel. Thus, when the designs are detailed for the production, the shell for the connecting region might require higher thermal resistance.

For the best-fit design, the COF #6 for Module 1 (Fig. 5.15) and that from the COF #4 for Module 2 (Fig. 5.16) are selected for their reasonable tradeoffs of the performance measures from both ends. For Module 1, the selected best-fit solution performs perform 28% better while compensating 41.5% of the structural performance as compared to the obtained solution for the COF #1, which has the highest structural performance among the obtained solutions; when compared to the solution for the COF#16 with the highest thermal performance among the obtained solutions, the selected best solution performs 1881.1% better in its structural performance while only compensating for 6.8% of its thermal performance. For Module 2, the selected solution has improved 17% of the thermal performance while compensating only 10.8% of the structural performance as compared to the solution for the COF#1; when compared to the solution for the COF#16, the selected solution has improved 2921.6% of the structural performance while compensating only 12.9% of the thermal performance.

| COF | $w_1$ | $w_2$ | $J_1$ | $J_2$ |
|---|---|---|---|---|
| **1** | 1 | 0 | 1254 | 32 |
| **2** | 1 | 1 | 1254 | 32 |
| **3** | 1 | 10 | 1254 | 32 |
| **4** | 1 | 50 | 1169 | 34 |
| **5** | 1 | 60 | 1143 | 35 |
| **6** | 1 | 70 | 733 | 41 |
| | | ... | | |
| **11** | 1 | 300 | 733 | 41 |
| **12** | 1 | 400 | 294 | 42 |
| **13** | 1 | 450 | 178 | 43 |
| **14** | 1 | 500 | 178 | 43 |
| **15** | 1 | 600 | 156 | 43 |
| **16** | 0 | 1 | 37 | 44 |

***Table 5.2:*** *Objective values of optimized solutions for the COFs in Module 1.*

| COF | $w_1$ | $w_2$ | $J_1$ | $J_2$ |
|---|---|---|---|---|
| **1** | 1 | 0 | 1254 | 46 |
| **2** | 1 | 1 | 1254 | 46 |
| **3** | 1 | 10 | 1249 | 47 |
| **4** | 1 | 50 | 1118 | 54 |
| **5** | 1 | 60 | 1118 | 54 |
| **6** | 1 | 70 | 1128 | 53 |
| 7 | 1 | 150 | 739 | 56 |
| **8** | 1 | 175 | 676 | 58 |
| **9** | 1 | 200 | 688 | 58 |
| **10** | 1 | 250 | 688 | 58 |
| **11** | 1 | 300 | 688 | 58 |
| **12** | 1 | 400 | 407 | 57 |
| **13** | 1 | 450 | 407 | 57 |
| **14** | 1 | 500 | 78 | 62 |
| **15** | 1 | 500 | 78 | 62 |
| **16** | 0 | 1 | 37 | 62 |

***Table 5.3***: *Objective values of optimized solutions for the COFs in Module 2.*

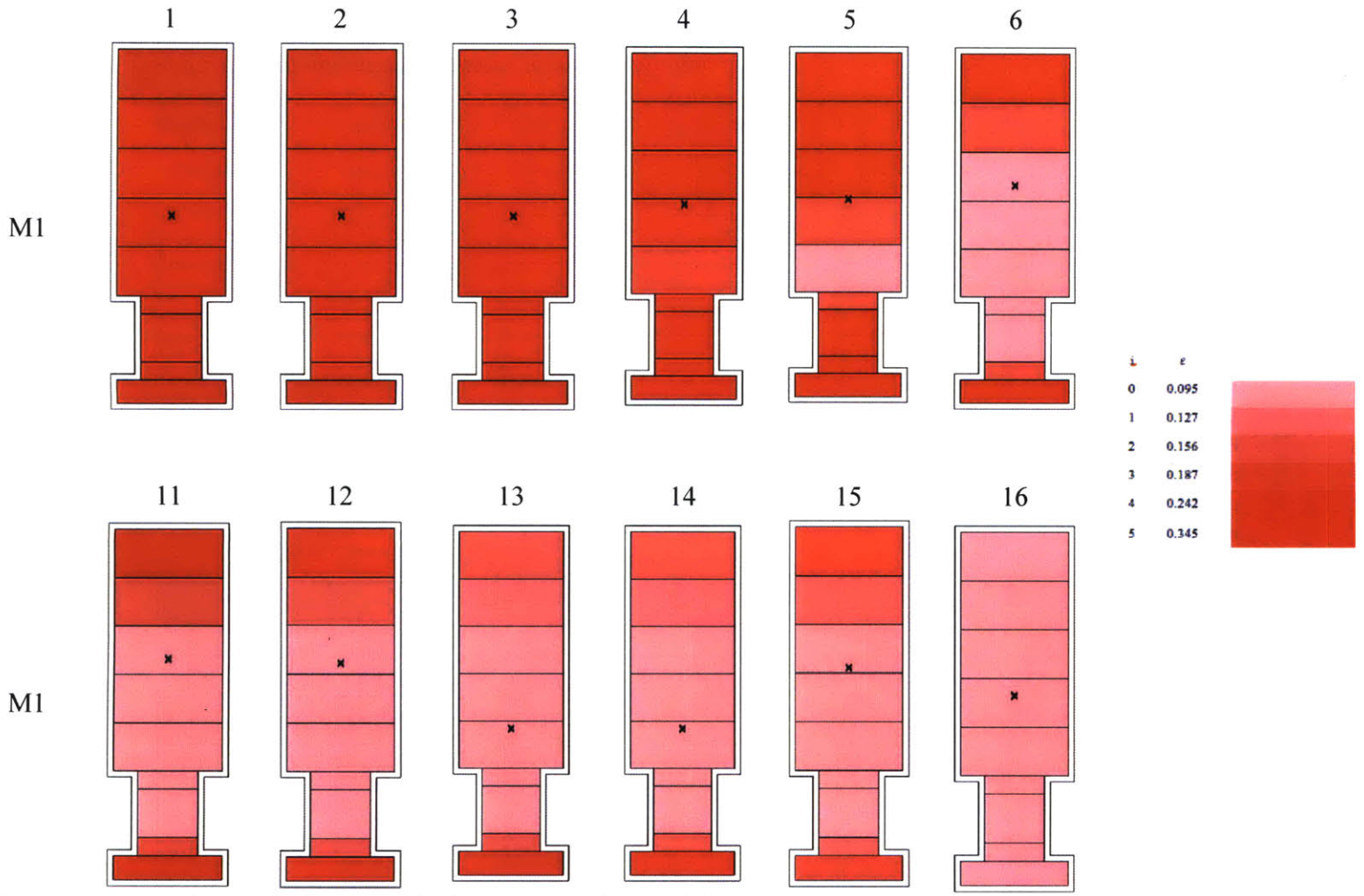


***Figure 5.12**: Visualization of optimized solutions found for Module 1.*

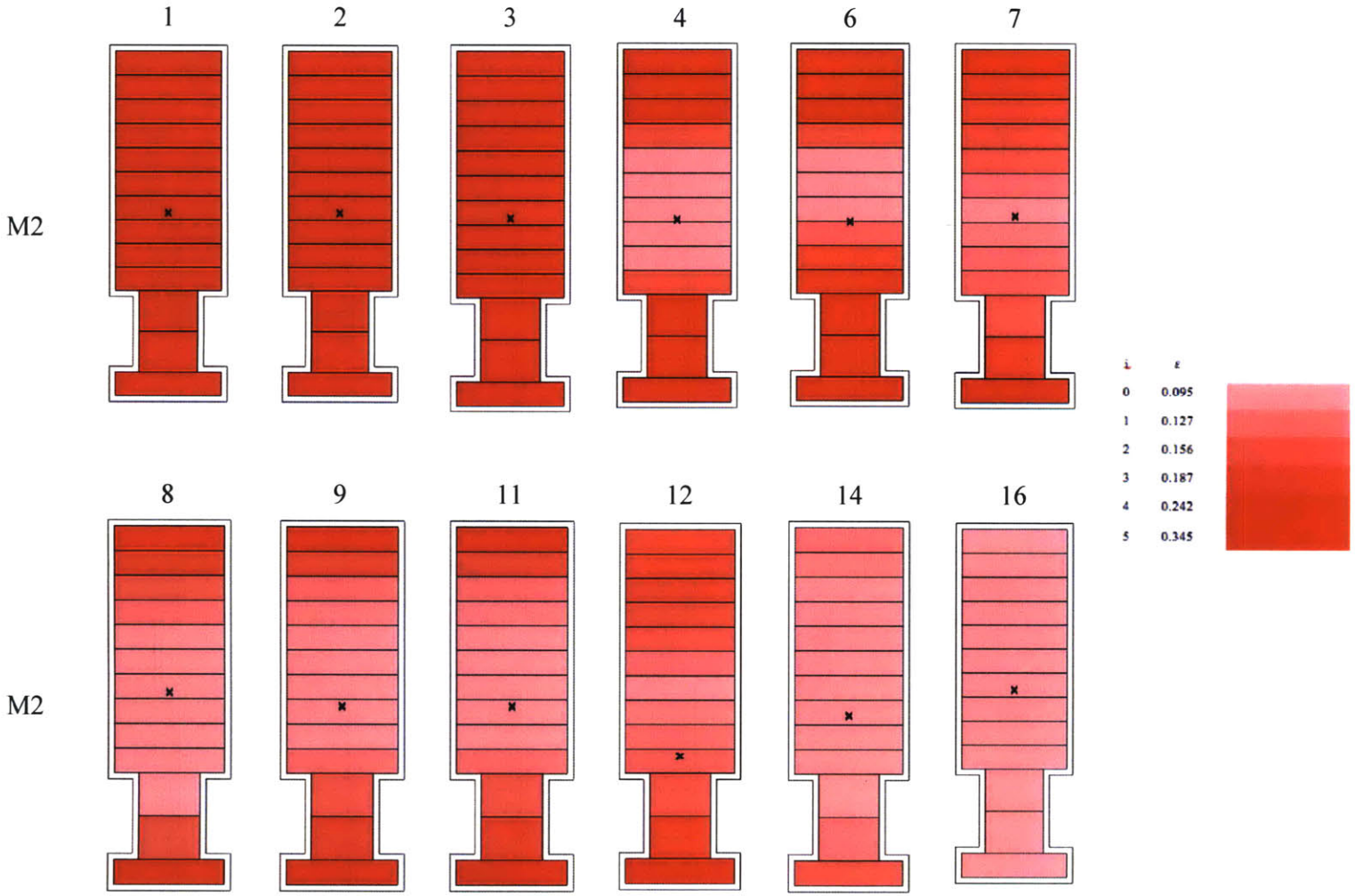


***Figure 5.13**: Visualization of optimized solutions found for Module 2.*

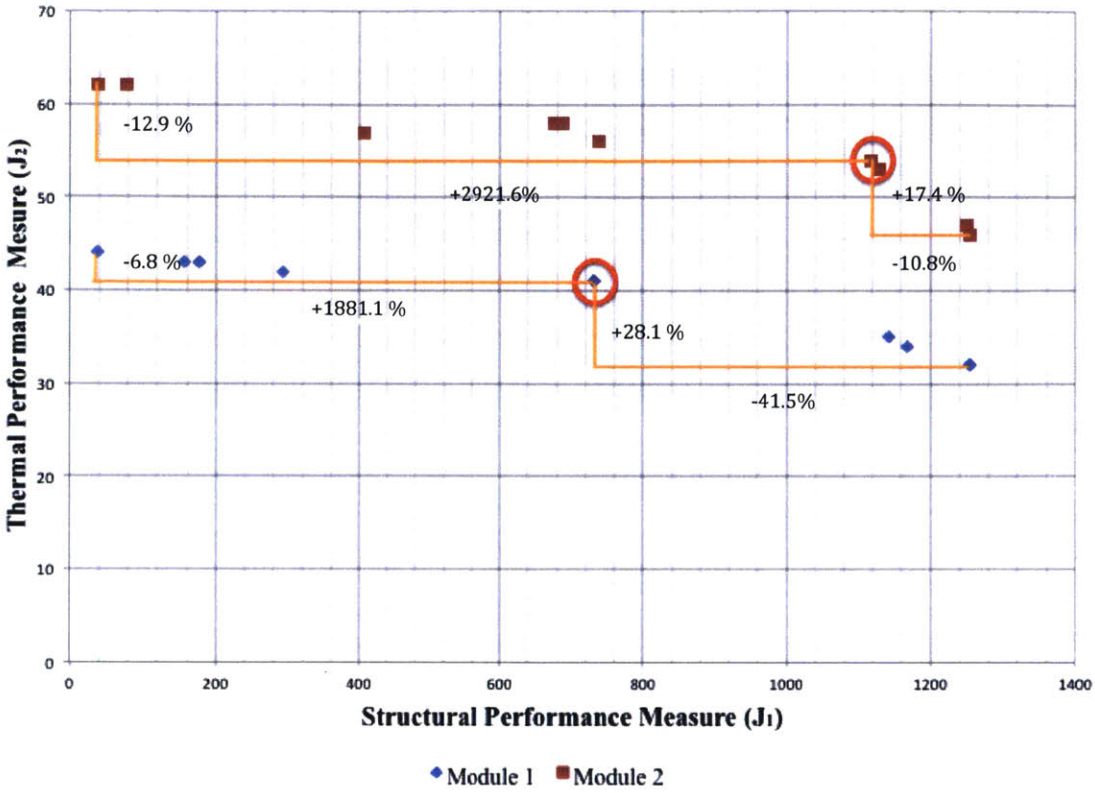


***Figure 5.14**: Plotted objective space for Module 1 and 2: selected optimized solutions in red circles.*

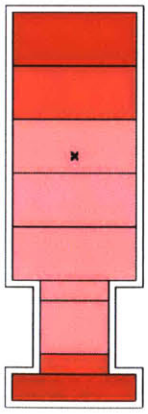

***Figure 5.15**: Selected topology as an optimized solution for Module 1.*

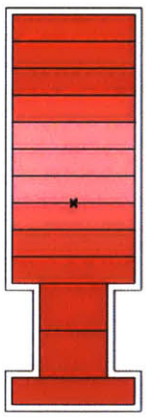

***Figure 5.16**: Selected topology as an optimized solution for Module 2.*

## 5.5. Summary

The design optimization of the composite gyroid structure for curtain wall mullion is carried out with the properties of gyroid, which are obtained in Chapter 4. The results of the optimization process are comprehensible in that the denser gyroid will provide higher structural performance but also more conductive materials for the heat transfer. With a further development of the parameterized modeling method of the intermediate regions, the results are expected to be constructible and useful. For the results to be practical and applied to the commercial design, however, it would require experimental verification.

# Chapter 6. Conclusions

## 6.1. Summary of Contributions

A cellular solid structure, gyroid, is studied for its future application in curtain wall mullion façade design to improve both thermal and structural performance. This thesis develops a rapid modeling method for gyroid structures and explores topology design optimization of a bi-objective design space, which evaluates structural performance and thermal performance. The performance measures are based on the scaling relations for the structural and thermal properties of gyroid. The scaling relations are obtained from both experiments and theoretical equations for open cell foams. In the bi-objective optimization study, the resulted objective space reveals the tradeoffs of the thermal performance and the structural performance of the design.

## 6.2. Potential Impact

As the curtain wall system is widely used in the realm of seeking more sustainable building design, the performance of the components has become one of the important decision-making criteria in designing curtain wall system. An improvement in the mullion design will significantly enhance the performance of not only the façade but also the entire building. With the advanced 3D printing technology available in the current era, the cellular solids and gyroid in various scale are becoming more achievable; thus, the application of the gyroid in mullion design for its advantages in performance will be come more feasible. As the research on gyroid structure continues for its unique structural features, more design effects are expected for using gyroid, particularly in façade design.

## 6.3. Future Work

This thesis provides a base framework for the application study of gyroid for façade design. As to complete the design and analysis of the application, several areas require more in-depth analysis and future developments. First, the thermal conductivity of the composite gyroid structure with air-fills requires verification with experimental data. Secondly, the scale of the gyroid may need to be revised for possible advantages. In a

Nano-scale, radiation can be a major pathway for the heat to be transferred throughout the structure. However, if the structure can be produced on the smaller scale, or with thinner aluminum gyorid, the structure can be lighter and yet expected to be stiffer than typical thermal blocks. Thirdly, the actual final design of the mullion with the composite gyroid structure requires being physically produced. The 3D printing methods utilized in this thesis might have smaller print beds for the entire curtain wall size, but a smaller size of prototype might be able to be printed using the 3D printers. Additionally, in the studied models, the detailed connections are simplified; therefore, the connection in the mullion section where glass panels are connected requires more thorough study for the application to be realistic.

The effects of convection and radiation are disregarded in this study when calculating heat transfer in the composite gyroid structures within the mullion design. This assumption require further verification in that convection effects can be significant for the air movement in the cavity can be created.

Moreover, the material choice and the cellular structure selection can be further explored to improve the performance and practicality of the design. For instance, micro-truss, which is a lattice-based cellular geometry, can be applied to its open cell structure for a large-scale production. As briefly mentioned in Chapter 2, the material choice for the gyroid is not explored to the full extent in this study. As with the Ashby chart on material vs. its mechanical properties and thermal properties, one can explore different materials for curtain wall design application for a further improvement in performance.

## 6.4. Concluding Remarks

This thesis suggests an application of gyroid sturcture in curtain wall mullion design to improve its stiffness and thermal resistance. The developed, digital modeling method has enabled a rapid modeling of the gyroid structures, and the results of the mechanical testing and obtained theoretical values help establishing better understanding of gyroid. The optimization results of this thesis and any further developments can better insist designers and engineers to advance the curtain wall design to be more energy-efficient.

# Chapter 7. References


Aluminum Association. 2000. *Aluminum design manual : specifications & guidelines for aluminum structures*. Washington, D.C.: Aluminum Association.

American Architectural Manufacturers Association. 1996. *Curtain wall design guide manual*. Palatine, Ill.: American Architectural Manufacturers Association.

Ashby, Michael F. 2000. *Metal foams: a design guide*. Boston: Butterworth-Heinemann.

Belova, Irina V. and Graeme E. Murch. 2008. "Thermal Properties of Composite Materials and Porous Media: Lattice-Based Monte Carlo Approaches." *Cellular and porous materials : thermal properties simulation and prediction*, edited by Öchsner, Andreas, G. E. Murch, and Marcelo J. S. de Lemos, 73-95. Weinheim : Wiley-VCH.

Brenden, Ken. 2006. "Dynamic Issues Drive Curtain Wall Design." *Structure Magazine*: 50-52.

Brock, Linda. 2005. *Designing the exterior wall: an architectural guide to the vertical envelope*. Hoboken, N.J.: John Wiley.

Bruggi, Matteo, Carlo Cinquini, and Alberto Taliercio. 2013. "Topology optimization of masonry blocks with enhanced thermomechanical performances." In *Proceedings of the 10th world congress on structural and multidisciplinary optimization, Orlando, Florida, USA*. http://www2.mae.ufl.edu/mdo/Papers/5173.pdf

Carbary, L. D., and A. Fiby. 2007. "A thermal modeling comparison of typical curtainwall glazing systems." Proceedings of Glass Processing Days 2007 (GPD): 282-286.

Carmody, John. 2004. *Window systems for high-performance buildings*. New York: Norton.

Çengel, Yunus A., and Afshin J. Ghajar. 2015. *Heat and mass transfer : fundamentals & applications*. n.p.: New York, N.Y. : McGraw-Hill.

Clyne, T. W., and F. Simancik. 2000. *Metal matrix composites and metallic foams*. [Germany] : Deutsche Gesellschaft für Materialkunde ; Weinheim ; Chichester ; New York : Wiley-VCH.

Coquard, R., Lorets, M. and Bailis, D. 2008. "Conductive heat Transfer in Metallic/Ceramic Open-Cell Foams." *Advanced Engineering Materials*, 10: 323-337. doi:10.1002/adem.200700331.

Dassault Systems. 2014. Abaqus 6.14.

Deaton, Joshua David. 2014. "Design of Thermal Structures using Topology Optimization." PhD diss., Wright State University.

DeGanyar, TJ. 2012. "Optimization in Component Design." *Insight* 02: 89-97. http://www.enclos.com/assets/docs/Enclos_Insight_02.pdf.

Engineering360. 2016. "Ceramic Matrix Composites Information." Accessed August 9. http://www.globalspec.com/learnmore/materials_chemicals_adhesives/ceramics_glass_materials/ceramic_matrix_composites.

Gibson, Lorna J., and Michael F. Ashby. 1997. *Cellular solids: structure and properties.* 2nd ed. Cambridge; New York : Cambridge University Press.

Glo Windows. 2016. "What Is A Thermal Break In Windows?" Accessed August 9. https://glowindows.com/what-is-a-thermal-break-in-windows/.

Harman, Jay. 2013. *The shark's paintbrush : biomimicry and how nature is inspiring innovation.* Ashland, Oregon : White Cloud Press.

Heumann, Andrew. 2010. Mesh to BRep.ghx. http://www.grasshopper3d.com/forum/topics/obj-into-brep?commentId=2985220:Comment:130347.

Kamiuto, Kouichi. 2008. "Modeling of Composite Heat Transfer in Open-Cellular Porous Materials at High Temperatures." *Cellular and porous materials : thermal properties simulation and prediction*, edited by Öchsner, Andreas, G. E. Murch, and Marcelo J. S. de Lemos,165-198. Weinheim: Wiley-VCH.

Kawneer. 2016. "2500 UT Unitwall System" Accessed August 9. http://www.kawneer.com/kawneer/north_america/en/product.asp?cat_id=1463&prod_id=4506&desc=insulated-curtain-wall-systems.

Lane, John. 1992. *Aluminium in building.* Aldershot, Hants, England ; Brookfield, Vt., USA : Ashgate.

Lee, Woo-Hyoung, and Jitiho Park. 2015. "A Study on Optimizing Shading Device Configuration for Glass Curtain Wall Buildings." Advanced Science and Techonology Letters 89: 5-8.

Martin, Randy L. 2013. "R-Value Table: Insulation Values for Selected Materials." ColoradoENERGY.org. Accessed August 8 2016. http://www.coloradoenergy.org/procorner/stuff/r-values.htm.

Mathworks. 2015. MATLAB_R2015b.

MeshLab. 2014. MeshLab v1.3.3. Retrieved from https://www.meshlab.sourceforge.net/.

Michalatos, Panagiotis and Sawako Kaijima. 2014. Millipede. http://www.sawapan.eu/.

Moczydlowski, Seth. 2015. "Gyroid: Modeling And 3d Printing." Accessed August 8. http://moczys.com/2015/04/06/gyroid-modeling-and-3d-printing/

Pawlyn, Michael. 2011. *Biomimicry in Architecture*. London : Riba Publishing.

Payette Research. 2014. "Thermal Performance of Facades." Accessed October 29, 2015. http://www.payette.com/post/2365186-thermal-bridging-research-curtain-walls.

Piacentino, Guilio. 2009. Weaverbird – 0.9.0.1. http://www.giuliopiacentino.com/weaverbird/.

Qin, Zhao, Gang Seob Jung, Min Jeong Kang, Markus J. Buehler. 2016. "The mechanics and design of light-weight three-dimensional graphene assembly." *Science Advances.* Manuscript.

Qin, Zhao. 2016. A MATLAB script for gyroid.

Robert McNeel & Associates. 2015. Grasshopper WIP. Retrieved from https://www.grasshopper3d.com

Robert McNeel & Associates. 2015. Rhino 5.0.

Scherer, Maik Rudolf Johann. 2013 "Gyroid and Gyroid-Like Surfaces." In *Double-Gyroid-Structured Functional Materials*, pp. 7-19. Springer International Publishing.

Schoen, Alan H. 1970. "Infinite periodic minimal surfaces without self-intersections." NASA Tech Note D-5541. Retrieved from http://citeseerx.ist.psu.edu/viewdoc/download?doi=10.1.1.115.3277&rep=rep1&type=pdf

Seitzberger, Markus, Franz G. Rammerstorfer, Hans Peter Degischer, and R. Gradinger. 1997. "Crushing of axially compressed steel tubes filled with aluminium foam." *Acta Mechanica* 125, no. 1-4: 93-105.

Seitzberger, Markus, Franz G. Rammerstorfer, Hans Peter Degischer, and R. Gradinger. "Crushing of axially compressed steel tubes filled with aluminium foam." *Acta Mechanica* 125, no. 1-4 (1997): 93-105.

Seitzberger, Markus, Franz G. Rammerstorfer, R. Gradinger, H. P. Degischer, M. Blaimschein, and Ch Walch. 2000. "Experimental studies on the quasi-static axial crushing of steel columns filled with aluminium foam." International Journal of Solids and Structures 37, no. 30: 4125-4147.

Singh, Ramvir. 2008. "Thermal Conduction Through Porous Systems." *Cellular and porous materials : thermal properties simulation and prediction*, edited by Öchsner, Andreas, G. E. Murch, and Marcelo J. S. de Lemos, 199-238. Weinheim : Wiley-VCH.

Smith, Geoffrey B., and Claes G. Granqvist. 2011. *Green nanotechnology : solutions for sustainability and energy in the built environment*. Boca Raton, FL : CRC Press.

SolaRoof. 2016. "SolaRoof: Sola Roof Tech." Accessed August 8. http://solaroof.org/wiki/SolaRoof/SolaRoofTech.

Starmark Windows. 2016."Bay or Bow Windows." *Starmark Windows*. Accessed August 9. http://www.starmarkwindows.com/products/bay-or-bow.stml.

Stattmann, Nicola. 2003. *Ultra light-super strong : neue Werkstoffe für Gestalter = Ultra light-super strong : a new generation of design materials*. Basel; Boston : Birkhauser Verlag für Architektur.

Stratasys. 2016. "PolyJet Materials Data Sheet." Retreived from http://usglobalimages.stratasys.com/Main/Files/Material_Spec_Sheets/MSS_PJ_PJMaterialsDataSheet.pdf?v=635785205440671440

Straube, John. 2008. "Can highly glazed building Façades Be green." Building Science Insights, BSI-006, https://www.buildingscience.com.

Syed, Asif. 2012. *Advanced building technologies for sustainability*. Hoboken, N.J.: John Wiley & Sons.

Szyniszewski, Stefan. 2016. "Research: Metallic Foam Sandwich Panels." Accessed August 9. http://www.szyniszewski.com/research/

Takezawa, Akihiro, Gil Ho Yoon, Seung Hyun Jeong, Makoto Kobashi, and Mitsuru Kitamura. 2014. "Structural topology optimization with strength and heat conduction constraints." *Computer Methods in Applied Mechanics and Engineering* 276: 341-361.

West, Heather. 2015. "Tubelite expands Therml=Block product offering, introduces TU24650 storefront." *2016 Tubelite Inc.* Accessed August 9. http://www.tubeliteinc.com/tubelite-expands-thermlblock-product-offering-introduces-tu24650-storefront/.

Winter, Benjamin, Benjamin Butz, Christel Dieker, Gerd E. Schröder-Turk, Klaus Mecke, and Erdmann Spiecker. 2015. "Coexistence of both gyroid chiralities in individual butterfly wing scales of *Callophrys rubi*." edited by Eli Yablonovitch *Proceedings of the National Academy of Sciences of the United States of America*. Vol. 112 no.42. doi: 10.1073/pnas.1511354112.

Wohlgemuth, Meinhard, Nataliya Yufa, James Hoffman, and Edwin L. Thomas. 2001."Triply periodic bicontinuous cubic microdomain morphologies by symmetries." *Macromolecules* 34, no. 17: 6083-6089.

Zeljic, Aleksandar S. 2010. "Shanghai Tower-Façade Design Process." In the 2010 International Conference on Building Envelope Systems and Technologies (ICBEST 2010) Retrieved from: http://www. gensler. com/uploads/documents/Shanghai_Tower_Faca de_Design_Process_11_10_2011. pdf.

Zienkiewicz, O. C., Robert L. Taylor, and Perumal Nithiarasu. 2014. *The finite element method for fluid dynamics*. Oxford : Butterworth-Heinemann.